2013

Low Strain Rate Studies Of Alumina Epoxy Composites Using Piezospectroscopy

Ashley Jones
University of Central Florida

LOW STRAIN RATE STUDIES OF ALUMINA-EPOXY COMPOSITES USING PIEZOSPECTROSCOPY

by

Ashley S. Jones
B.S. University of Central Florida, 2011

A thesis submitted in partial fulfillment of the requirements
for the degree of Master of Science
in the Department of Mechanical and Aerospace Engineering
in the College of Engineering and Computer Science
at the University of Central Florida
Orlando, Florida

Spring Term
2013

Major Professor:
Seetha Raghavan

Abstract

Particulate composites are widely used in many aerospace and military applications as energetic materials, armor materials or coatings and their behavior under dynamic loads have gained increasing significance. The addition of modifiers such as alumina nanoparticles generally facilitates the improvement of the mechanical strength to density ratio due to high specific area and particle rigidity. This allows for sufficient particle-matrix bonding and therefore improved stiffness and load transfer in the composite. Photo-luminescent α-alumina nanoparticles when embedded in an epoxy matrix allow for the added benefit of in situ measurements at low strain rates to provide stress-sensitive information using the particle piezospectroscopic (PS) property. To investigate the low strain rate behavior, cylindrical specimens of alumina-epoxy composites with varying volume fractions of alumina were fabricated using a casting process to ensure minimal surface finishing and reduced manufacturing time. The results illustrate the capability of alumina nanoparticles to act as diagnostic sensors to measure the stress-induced shifts of the spectral R-line peaks resulting from low compressive strain rates. The range of PS coefficients measured, -3.15 to -5.37 cm^{-1}/GPa for R1 and -2.62 to -5.39 cm^{-1}/GPa for R2, correlate well with static test results of similar volume fractions. Results reveal a general trend of increasing sensitivity of the PS coefficients with increasing strain rate when compared to similar materials under static conditions. In contrast to static results, at a given strain rate, the PS coefficients show varying degrees of sensitivity for each

volume fraction. This information can be used to determine the time-dependent micro-scale stresses the nanoparticles sustain during composite loading. Additionally, this work facilitates failure prediction by monitoring upshifts in the PS information. Calibration of the in situ diagnostic stress sensing capabilities of varying volume fractions of alumina nanocomposites under quasi-static strain rates in this work sets the precedent for future studies at high strain rates.

This work is dedicated to my father whose continuous support and guidance has inspired me to become the person that I am today.

Acknowledgments

My sincere gratitude is extended to my research advisor and Thesis Chair, Dr. Seetha Raghavan, for the exceptional leadership, guidance, and understanding offered throughout this project. A special thank you is also extended to my committee members, Dr. Raj Vaidyanathan and Dr. Ali P. Gordon, for their participation, knowledgeable advice, and continued support. Recognition is given to following University of Central Florida students, Gregory Freihofer, Kevin Knipe, and Marc Lowen, for their combined encouragement, assistance, and communication of ideas. This work is supported by the University of Central Florida in house research grant and National Science Foundation Graduate Research Fellowship under Grant No. DGE-1144246.

TABLE OF CONTENTS

LIST OF FIGURES

LIST OF TABLES

CHAPTER 1
INTRODUCTION

1.1 Motivation and Background

Reinforcing particles in a polymer binder are used in many military, aerospace, and civil applications for their ability to improve the overall material properties of the composite. Composites with reinforcing particles can be customized for desired mechanical properties with different matrix or filler materials, particle sizes, shapes, or volume content, and loaded under any condition [39, 71, 22, 59, 17, 1, 21, 82, 75, 76, 6, 3, 29, 85, 11, 9, 63]. In addition to the benefit of customization, particulate composites can have improved fatigue resistance, corrosion resistance, and lower manufacturing costs, which makes them very attractive when compared to their conventional metal counterparts [37]. The ability to customize and improve material properties have led particulate composites to be used in a wide range of configurations. Nanometer sized TiO_2 particles in an epoxy matrix have been used to increase composite scratch resistance [63], flexural strength, and toughness [80]. SiC has been used in various matrices to increase the strength of the composite [16], and aluminum particles have been introduced to epoxy to increase fracture toughness [87]. The contrast in rigidities offered by the particles and the matrix has benefits in providing energy dissipating properties which are utilized in applications for protection against micrometeorites for satellites and high-speed particle impact for jet engine turbine blades [51] in layered nanocomposites.

Ceramic nanocomposites, specifically, alumina particulate composites are becoming more widely used due to their low densities and relatively high strengths [40]. High stiffness-to-weight ratios due to increased particle rigidity also make alumina composites desirable as high surface areas allow for sufficient particle-matrix bonding and the improved stiffness facilitates load transfer to the particles. Statically, alumina particles have been used in adhesives [25, 50, 17] and as plasma sprayed coatings to improve the wear, thermal, electrical, and/or corrosion properties of machine components [20, 84]. Dynamic applications of alumina particulate composites include encapsulation of ferroelectric elements for shock depoling [53] and potting compounds for explosive and propellant tests [57, 18]. Various types of alumina composites have also been used as armor materials [15], where the durability and energy dissipating properties have proved beneficial.

In addition to improved mechanical properties, chromium doped α-alumina particles can offer additional diagnostic benefits through their photo-luminescent properties. Through the use of optical methods, such as piezospectroscopy, particle stresses and load transfer mechanics can be characterized through the piezospectroscopic (PS) coefficient by measuring the stress-induced shifts of the characteristic R-line peaks present in the emission spectrum of alumina, known as the PS effect as shown in Figure 1.1.

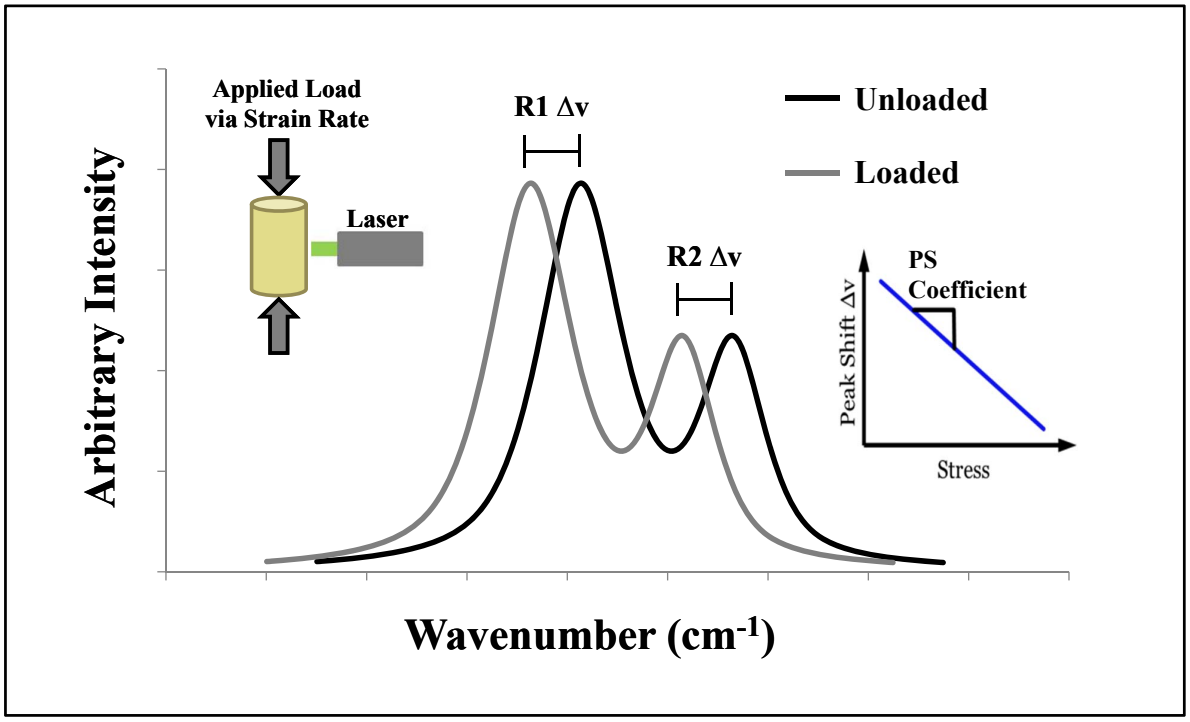

Figure 1.1: Piezospectroscopic effect

The emission of R-lines under laser excitation is due to the naturally occuring Cr^{3+} impurities in the crystal lattice of α-alumina and these lines are easily identified as two sharp and closely spaced peaks, known as R1 and R2. The application of the PS effect was first introduced to monitor pressure in diamond anvil cells [5] which verified the ability of these materials to capture stress-induced shifts of the R-line peaks. Further studies on chromium-doped sapphire [33] determined the PS coefficients, which is a measure of the sensitivity of the R-line shift with stress, followed by studies on polycrystalline ceramics [55, 67]. Piezospectroscopy of alumina-epoxy composites has been used to determine

the thermal stress distribution of encapsulated microelectronic devices [62] and for stress sensing calibration studies of variable volume fractions of alumina nanocomposites under static conditions [75, 77]. Static stresses have also been studied in the thermally grown oxide layer under thermal barrier coatings on jet engine turbine blades by utilizing the trace Cr^{3+} ions incorporated in the growing α-alumina scale [13, 12, 64, 24, 65, 74]. Dynamically, the behavior of ruby has been characterized under shock loading for the development of optical stress gages using the piezospectroscopic behavior of the material [32, 70, 30, 35]. The fast data collection times associated with emission data collection lend itself well to capturing material response under strain rates. Such measurements can be envisioned to produce new and significant information in the study of the dynamic response of particulate composites. One such application is the sensitivity of energetic materials to mechanical stimuli, which is sometimes studied through dynamic tests on non-reactive alumina-epoxy materials to experimentally assess the parameters affecting the reliable functioning of a munition and avoidance or mitigation of accidents [7].

The increased significance of particulate composites such as alumina-epoxy nanocomposites, motivates the need to develop these novel measurement techniques to understand the material behavior under various loading conditions, whether static, quasi-static, or dynamic conditions . Our previous studies have demonstrated the successful piezospectroscopic calibration of the static response of alumina particulate composites [75, 77]. This highlights the potential for this method to monitor loading under variable strain rates in many typical applications. Since the material behavior for many other types

of composites has been shown to vary significantly with strain rate [37], understanding the failure mechanics under variable strain rates is important for the design and safe use of these materials. The need to understand the mechanics of particulate composites such as alumina-epoxy nanocomposites coupled with the potential for high in-situ collection of strain information of this material using piezospectroscopy provides an excellent motivation for the variable strain rate studies initiated through this work.

1.2 Effect of Strain Rate on Mechanical Properites

The general variation in material response between static and dynamic loading in tension and compression is well-known and documented historically [2]. Outside the realm of static tests, the response of materials under quasi-static, low, and high strain rates can also differ substantially. For example, Law and Wilshaw concluded that the quasi-static and dynamic response during indentation tests did not correlate well [49, 15]. Many factors, including surface and friction effects, microcracking, and microplasticity, can affect the material response during increased loading rates. Specifically, the rate of load application has been found to influence the process of microcrack development [48]. With higher strain rates, the increased strain rate dependency is thought to arise from crack inertia, which is controlled through confining pressures [48].

Many fiber-reinforced polymer composites loaded in both tension and compression show an improved mechanical response to increased loading rates. Tensile glass/polyester

and glass/epoxy composite studies report an increase in tensile strength with increasing loading rate [37]. Compressive studies on carbon/epoxy [28], graphite/epoxy, glass/polymer, and glass/polyester all report an increase of compressive strength with increasing loading rate [37]. In a similar way, some multi-constituent particulate composites, such as aluminum/nickel/epoxy, have improved compressive strengths with increasing loading rates [42, 39, 43]. Low and high strain rate compressive tests on polycrystralline alumina reveal both increased compressive strength with loading rate and sensitivity regimes transitioning around $10^{-1}s^{-1}$ [46]. Several studies have investigated the effect of strain rate on the mechanical properties of alumina-filled epoxy composites. For example, micron-sized alumina particles added to epoxy at 37 and 43% volume achieve higher axial stresses at increased loading rates [59, 68]. Various volume fractions, including 20, 33, and 42% alumina in epoxy revealed increasing Hugoniot stress with increasing impact velocity [61]. Half and fully loaded alumina filled epoxy composites, approximately 20 and 42% volume fraction respectively, show a similar trend of higher axial stress with increasing strain rate [57], with the fully loaded composite achieving the highest stress values. The overall improvement in mechanical response of these materials under dynamic conditions points toward the strengthening mechanisms and interactions of the constituents at the microscale. This highlights the need to enable and develop measurements such as piezospectroscopy for strain rate studies to establish an understanding of the response.

1.3 Overview of Research

The improved mechanical properties at increased loading rates seen by the mechanical response and failure of these composites is often dominated by the particle-matrix and particle-particle interaction that leads to strengthening mechanisms in these materials. Understanding these interactions is difficult and deciphering the characteristics of composites from the properties of the individual components remains a significant and challenging problem [61]. Piezospectroscopic studies utilizing the characteristic photoluminescent alumina nanoparticles as "nano-sensors" within an epoxy matrix has the capability of providing substantial information with respect to the stresses experienced by the constituent particles. With the motivation of characterizing the effect of strain rate on the stress transfer characteristics at the microscale, in-situ measurements at quasi-static strain rates can be collected in order to elucidate the load transfer mechanics through particle piezospectroscopic (PS) behavior.

Chapter 2 outlines the theory and definition of the strain rate range used within this work and describes the behavior of materials, including alumina-epoxy composites, at various strain rates. The fundamentals behind the piezospectroscopic property of the material is introduced including relevant theory, process of data analysis, and curve fitting. Success of the method with both static and dynamic tests is discussed in order to show the reliability of the method to collect stress-sensitive information at the microscale and relate load transfer information through optical methods.

The mechanical effects of particle size, volume fraction, and aspect ratio are discussed in Chapter 3. The specimen fabrication is also discussed, along with the use of strain gages to collect strain information from the bulk composite material. Methods and measurements ensuring acceptable dispersion through intensity measurements, density calculations, and elastic modulus determination is also outlined in Chapter 3.

Results for the mechanical and piezospectroscopic analysis of varying volume fractions of alumina under quasi-static conditions is described in Chapter 4 and 5, respectively. Relevant findings are also discussed in Chapter 5. Finally, conclusions and future directions in this work are discussed in Chapter 6.

CHAPTER 2
MECHANICS OF STRAIN RATE TESTING AND PIEZOSPECTROSCOPY

2.1 Mechanics of Strain Rate Testing

2.1.1 Definition of Strain Rate Range

Strain rate regimes are typically characterized in different regions, that is, static, quasi-static, low, intermediate, and high. Static regimes are generally characterized by the absence of a loading rate or loading without progressive motion. However, dynamically, the regimes are usually characterized with varying definitions of the boundaries that distinguish them. For example, in studies on polycrystalline alumina, Lankford described three strain rate regimes, low on the order of $10^{-5}s^{-1}$, intermediate on the order of $10^{-1}s^{-1}$, and high on the order of $10^{3}s^{-1}$ [46]. On the other hand, Jordan described quasi-static strain rates on the order of 10^{-4} to $10^{-3}s^{-1}$ and intermediate strain rates on the order of $10^{3}s^{-1}$ in her work with aluminum/nickel/epoxy composites [39]. The strain rates employed in this work on alumina epoxy composites fall within the low strain rate definition generally described as quasi-static and are generally in the order of 10^{-4}, 10^{-3}, and $10^{-2}s^{-1}$.

2.1.2 Behavior of Materials at Various Strain Rates

Material behavior is affected by many factors including matrix and filler material, particle size, shape, or volume content, but has also been shown to be highly affected by the loading rate. Specifically, at increased rates of loading, many factors can affect the material response, including surface and friction effects, microcracking, inertial effects associated with motion of the microstructure, and microplasticity [18, 37]. According to Drumheller [18], the dynamic response of particulate loaded materials presents several challenges. First, contact between neighboring particles can transmit loads independently of the load carried by the filler material, which may dismiss the assumption of equal constituent pressures [18]. Second, the effective modulus of the particle matrix is a strong function of the confining pressure as particles can "lock" together under large confining pressures [18]. Third, distortion can result in dilation of the mixture due to the interference pattern set up between particles during a shearing motion of the particle matrix [18]. Lastly, finite deformation of the mixture is opposed by large internal frictional forces originating at the interparticle contact sites [18].

Lankford suggested that all ceramics fail in pure compression by the coalescence of multitiple axially-oriented microcracks [47]. Specifically, microstructural factors and inhomogeneities are known to be responsible for the local tensile stresses near grain boundaries that nucleate microcracks [47]. For quasi-static strain rates on the order of

10^{-5} to $15^{-1}s^{-1}$, it has been shown that the failure process obeys the following equation:

$$\sigma_c \propto \dot{\varepsilon}^{\frac{1}{(1+n)}} \tag{2.1}$$

where σ_c is the compressive strength, ε is the strain rate, and n is equal to the stress intensity exponent in the macroscopic tensile crack velocity relationship [47]. This process dominates several common ceramics, such as SiC, Al_2O_3, and Si_3N_4 and is relatively strain rate insensitive. However, at higher loading rates, the dependence of strength on strain rate is much more sensitve. For strain rates in the range of 10^3 to $10^4 s^{-1}$, the dependence is described by the following equation:

$$\sigma_c \propto \dot{\varepsilon}^{\frac{1}{3}} \tag{2.2}$$

At much higher strain rates, such as $10^6 s^{-1}$, microsplasticity dominates the material response, where blocked plastic flow induces grain boundary stress concentrations and microfracture or slip, in cases where the grain boundaries are relatively clean [47]. In compression, the strain rate strengthening effect persists at much higher strain rates due to stablization of microcracks under compressive loads [46]. On the other hand, under tensile loading at increased strain rates, the critical stress intensity for failure is attained at the tips of growing cracks and tensile falure becomes insensitive to further strain rate increases [46].

At high strain rates, a sudden change in velocity causes a shock wave to travel through the material [19]. At the limiting factor, the stress behind the shock is known as the Hugoniot elastic limit (HEL), however, past the limiting factor, the material exhibits

a response much different than in the region before the limit as two shock waves are produced. This response is characterized by the Rayleigh line, where the region before and after the HEL are straight lines with two different slopes. The jump in stress, due to the shock, cause a leading and trailing shock wave, called the elastic precursor and plastic shock wave respectively, to form before and after the HEL. For values that greatly exceed the limiting factor, it is possible that the elastic precursor can be "overdriven" by the plastic shock wave [19]. Regions before and after the HEL do not behave similarly for elastic-plastic materials, therefore, care must be taken to ensure appropriate regions of strain rates for comparison. While the region of strain rates addressed by the experiments in this work covers the low strain rate range, it is envisaged that the methods and approach taken in these studies can be extended in future studies to investigate the significant events and response of the material that take place at high strain rates.

2.1.3 Polycrystalline/Ruby and Alumina-Epoxy Composites at Various Strain Rates

The mechanical response of polycrystalline alumina has been studied under high strain rates. It has been documented that the HEL increases with decreasing grain size, characterized by a linear behavior, and is roughly 12 GPa for grain sizes in the 1 micron range [60]. At impact stress values below the HEL, the microstructure shows clear evidence of failure along the grain boundaries and above the HEL, grains show twinning,

where crystals share lattice points [8]. Alumina has a three zone response, elastic, mixed-response, and inelastic region, each separated by a lower and upper HEL [8]. The lower HEL corresponds to the region of the onset of twinning in suitable grains [8]. Complete twinning occurs in the upper HEL region which leads to intragranular fracture along twin boundaries and fast grain fracture limited only by the speed of crack propagation at pressure [8]. Polycrystalline alumina was shown to have a strength dependence on strain rate in the region of 10^{-4} to $10^{3}s^{-1}$, with varying slopes between each endpoint and roughly $10^{-1}s^{-1}$ [46]. The rate of load application has been found to influence the process of microcrack development [48]. With higher strain rates, the increased strain rate dependency is thought to arise from crack inertia, which is controlled through confining pressures [48]. Additionally, ruby, with a reported HEL of 14 GPa, has also been studied under shock compression where higher stresses were achieved at increased loading rates [45, 32]. Values for ruby in the elastic region have been reported up to 12.56 GPa [45].

Composites based upon particulate reinforcement can be considered isotropic [57]. Alumina-epoxy composites with 43% volume fraction of micron-sized particles are characterized by an HEL of 3 GPa under shock compression for velocities between 0.42 and 0.91 km/s [68]. Therefore, given an applied range of shock stress up to a maximum point near HEL, it has been assumed that alumina responds in a purely elastic way. In contrast, the epoxy binder may be assumed to respond inelastically at higher shock stresses [57]. Studies on alumina epoxy composites with 20, 33 and 42% filler material revealed an

increasing Hugoniot stress with strain rate [61] as determined by the Maxwell model, a rate-dependent differential equation used to calculate the stress-wave propagation in Al_2O_3 composites.

2.2 Piezospectroscopy

An added benefit to the mechanical property characterization presented in this study, is the ability to use photo-stimulated luminescence spectroscopy (PSLS) to measure the stress-induced shifts of the R-line peaks present in the emission spectrum of chromium-doped α-alumina as shown in Figure 1.1. Relevant to work with ruby, polycrystalline alumina, and bulk alumina-epoxy composites, laser excitation causes the Cr^{3+} ions in alumina to transition from an exicited state back down to a ground state, where photons are emitted at set wavelengths to form the characteristic R-lines. The piezospectroscopic (PS) effect, introduced by Grabner [27] relates the frequency shifts in the fluorescence spectrum of the R-lines to applied stress as shown by the following equation:

$$\Delta\nu = \pi_{ij}\sigma_{ij} \tag{2.3}$$

where $\Delta\nu$ is the frequency shift, π_{ij} represents the piezospectrocopic coefficient, and σ_{ij} is the stress state as defined by the crystallographic frame of reference. However, the frequency shift of a fluorescence line in a luminescing crystal oriented at an arbitrary angle to a superimposed stress and strain field is given by the following tensorial relation [54,

34]:

$$\Delta\upsilon = \pi_{ij} a_{ik} a_{jl} \sigma_{kl} \tag{2.4}$$

where π_{ij} represents the piezospectrocopic coefficient, a_{ij} is the transformation matrix, and σ_{kl} is the stress state. Ma and Clarke derived an equation for the frequency shift of fluorescence lines, irrespective of the crystal structure, from a large number of randomly oriented grains in a polycrystalline material as shown below [54]:

$$\overline{\Delta\upsilon} = \frac{1}{3}(\pi_{11} + \pi_{22} + \pi_{33})(\sigma_{11} + \sigma_{22} + \sigma_{33}) \tag{2.5}$$

By neglecting tranverse stress ($\sigma_{33} = 0$) and assuming equal in plane stresses ($\sigma_{11} = \sigma_{22} = \sigma$), the above equation can be expressed as follows:

$$\overline{\Delta\upsilon} = \frac{2}{3}(\pi_{11} + \pi_{22} + \pi_{33})\sigma \tag{2.6}$$

For the case of alumina nanoparticles embedded within an epoxy matrix, the frequency shift of the R-lines collected from the alumina particles and applied stress can be directly related to the PS coefficient for the nanocomposite as shown in the following expression:

$$\Delta\nu = \Pi_{NC}\sigma_{applied} \tag{2.7}$$

where $\Delta\nu$ is the frequency shift of the peak position of the fluorescence line of the embedded alumina nanoparticles, Π_{NC} is the PS coefficient of the nanocomposite, and $\sigma_{applied}$ is the stress applied to the nanocomposite. By using this equation, the particle behavior is able to be distinguished from the matrix behavior. Therefore, determining the

elasticity of the particles in relation to the inelasticity of the matrix is possible through direct measurement of the load transfer to the much stiffer particle modifiers.

2.2.1 Deconvolution and Curve Fitting

As a consequence of alumina luminescence, the R-lines share a region of data that contributes to peak positions affected by convolution in raw experimental data as shown in Figure 2.1.

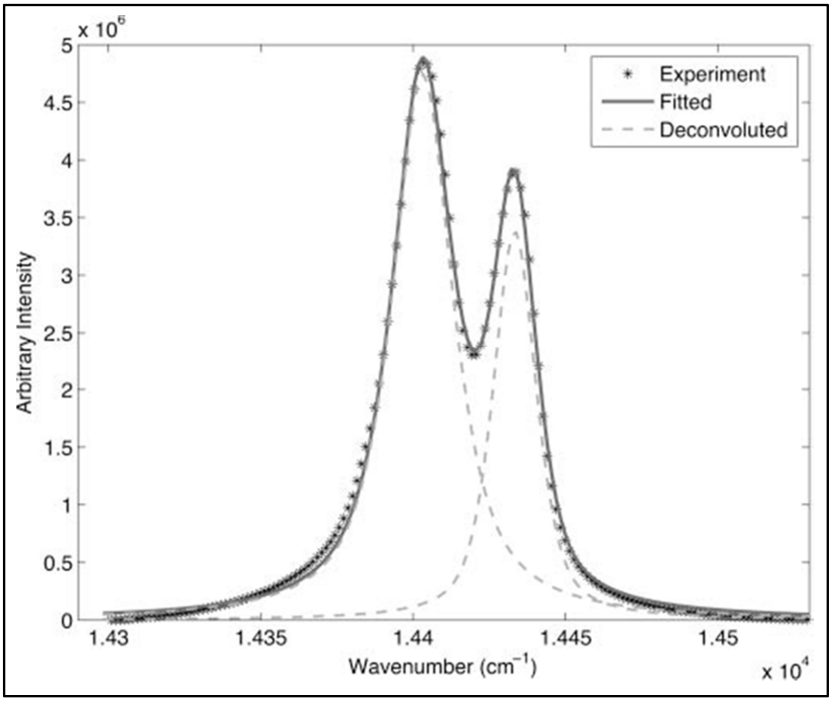

Figure 2.1: Deconvolution and curve fitting [66]

Therefore, the raw experimental data must undergo a deconvolution and curve fitting procedure to ensure accurate peak positions, and thus, accurate peak position shifts. Previously used to correct the R-line peaks for polycrystalline alumina [66] and alumina nanoparticles embedded in an epoxy matrix [75], a genetic algorithm (GA) based procedure [23] was also used in this work on the raw experimental data.

As opposed to gradient-based methods, this GA method has the capability of global optimization [81, 14] and is utilized while performing four main functions on unprocessed data: baseline removal, curve cropping, curve separation, and curve recombination. This optimization is accomplished by two pseudo-Voigt functions [44, 78, 36] which obtain several important parameters for the R1 and R2 lines such as area, line-widths, peak position, peak intensity, and goodness of fit. After the curve fitting procedure, the true peak positions of the R-lines are realized, R-line shifts can be calculated, and piezospectroscopy can be utilized to determine the PS coefficients and resulting load transfer characteristics.

2.2.2 Success with Static Measurements

Piezospectroscopy has been successfully used to determine the load transfer mechanics for ruby, polycrystalline alumina, and alumina-epoxy composites. Many studies have investigated the effect of applied stress on the shift of luminescence lines, including work by He and Clarke, Raghavan, Ma and Clarke, and Stevenson. He and Clarke's work

determined the PS coefficients for ruby under uniaxial compressive stress and developed the following relationships for the frequency shift of the R-lines in terms of the three crystallographic directions [34]:

$$\Delta\nu\left(R_1\right) = 2.56\sigma_{11} + 3.50\sigma_{22} + 1.53\sigma_{33} \tag{2.8}$$

$$\Delta\nu\left(R_2\right) = 2.65\sigma_{11} + 2.80\sigma_{22} + 2.16\sigma_{33} \tag{2.9}$$

The effects of stress on the peak position shifts for ruby under uniaxial compressive stress was also investigated by Raghavan [66]. With the use of a GA based procedure, the PS coeficients for the a, c, and m axis for R1 were reported as 2.65, 2.83, and 1.51 cm^{-1}/GPa. Raghavan also measured the stress induced shifts of the R-line peaks for polycrystalline alumina with reported values of 2.64 and 2.47 cm^{-1}/GPa for R1 and R2, respectively [67].

Ma and Clarke investigated the effect of stress on the peak shift and broadening of the R1 and R2 lines for polycrystalline alumina [54] using a four point bending stage to capture both tensile and compressive stresses. Their work determined the shift dependence on stress as 2.46 and 2.50 cm^{-1}/GPa for R1 and R2 using the least-squares analysis and 2.53 and 2.54 cm^{-1}/GPa for R1 and R2 using the hydrostatic pressure dependence [54].

Alumina-epoxy composites of varying volume fractions of 5, 25, and 38% α-alumina nanoparticles were investigated by Stevenson [75] in order to develop stress-sensing adhesives using piezospectroscopy. Results for this study revealed increasing sensitivity to load transfer as seen by increasing PS coefficients with increasing volume fraction.

Specifically, the magnitude of PS coefficients were reported for R1 as 3.16, 3.65, and 5.63 cm^{-1}/GPa for 5, 25, and 38% alumina, respectively. Additionally, collected photoluminescent intensity information was used to verify composite dispersion, regions of voids, and areas of localized stress concentrations.

2.2.3 Strain Rate Studies using Piezospectroscopy

Dynamically, the behavior of ruby has been characterized under shock loading using the piezospectroscopic behavior of the material. Horn and Gupta analyzed the wavelength shift of ruby luminescence lines under shock compression using impact experiments with a single stage gas gun [35]. This produced a state of uniaxial strain in the material using two pressures, 40 and 99 $kbar$. Results revealed an upshift in wavelengths between 0-25 nm plotted against density compression as represented by the following equation:

$$Density_{compression} = \frac{\rho}{\rho_o} \tag{2.10}$$

An upshift in nm correlates to a downshift in cm^{-1} as would be expected for compressive loading. Gupta also performed experiments on ruby under shock compression in order to develop optical stress gages [31]. This work utilized impact experiments with particle velocities of 0.117-0.200 $mm/\mu s$. R1 peak shifts for ruby were reported in the range of 11.9 to 22.5 $\mathring{A}$ with longitudinal stresses of 52.5 to 91 $kbar$. These shifts can be represented as downshifts in cm^{-1} also plotted against density compression as de-

fined above. In both studies of ruby, the mechanical quantities were calculated using the sapphire Hugoniot and Rankine-Hugoniot jump conditions [31].

In another study, Shen and Gupta investigated the ruby R-line shifts for high pressure calibration [30]. These experiments utilized a single-stage, compressed gas gun to achieve impact velocites of 200-600 m/s, which imparted stresses between 25 and 125 $kbar$. Upshifts in $\mathring{A}$ were plotted against both density compression and mean stress ($kbar$) for R1 and R2, which would correlate to downshifts if represented in cm^{-1}. An important finding of this work is the insensitivity of the R2 shift to crystal orientation and non-hydrostatic stresses, with dependence only on density compression [30].

CHAPTER 3
SPECIMEN GEOMETRY, FABRICATION, MATERIAL PROPERTY DETERMINATION, AND EXPERIMENTAL SETUP

3.1 Mechanical Effects of Particulate Reinforcements

3.1.1 Particle Modifiers

In comparison to metal materials, an un-reinforced polymer will exhibit inferior mechanical properties such as strength and poor resistance to crack initiation and propagation. Therefore, it is imperative that polymers be reinforced with particle modifiers to improve mechanical properties of interest. High stiffness-to-weight ratios due to increased particle rigidity make particle modifiers desirable and high surface areas allow for sufficient particle-matrix bonding.

Silica [38, 4, 10], titanium oxide [80, 22], and aluminum oxide [25, 72, 86, 79, 56], also known as alumina, are some of the more commonly used fillers. Ceramic reinforcing particles have been used in lightweight armor applications to improve mechanical impact properties [52, 69, 58, 73, 72, 16, 87] and in adhesive applications to improve adhesion, toughness, and peel strength [25]. Specifically, alumina modifiers are becoming more widely used in epoxy due to the relatively low densities and high strengths [40] of the resulting composite.

When compared to micron-sized particles, nanoparticles offer higher surface-to-volume ratios [26], which allow for improved bonding between filler and matrix material. Nano-

sized modifers also show superior crack resistance over micron-sized particles. The rigid particles serve as barriers that the crack must traverse in order to propagate, thus impeding growth. Ultimately, these modifiers serve as reinforcing agents to the matrix material by improving composite stiffness and increasing particle-matrix surface bonding area, and typically, do not have an adverse impact on mechanical properties of the composite [83].

3.1.2 Volume Fraction

Particle modifiers have been shown to have offer substantial improvements to mechanical properties of interest, however, the amount of filler content, or volume fraction, also has an effect the mechanical response of the composite. Lower volume fraction composites are typically dominated by the matrix behavior and higher volume fractions are usually much stronger, but are notoriously more difficult to manufacture. Studies directly relating the amount of filler material to improvements in mechanical properties have been performed and are important as the amount of filler material should be minimized in order to reduce cost and waste, while maximizing mechanical performance. One such study, which investigated nano-alumina modified epoxy based film adhesives, determined that 10% of nanoparticles by weight is the maximum amount that could be added while still maintaining even dispersion [25]. However, in stress-wave propagation studies for alumina-epoxy composites, it has been shown that 43% α-alumina is the maximum amount that can

be added to an epoxy without reducing the overall mechanical properties of the epoxy itself [61].

Higher volume fractions have been shown to have superior load transfer to the particles in studies of alumina-epoxy composites under static conditions [75, 77]. The load transfer mechanics can be visualized by Figure 3.1.

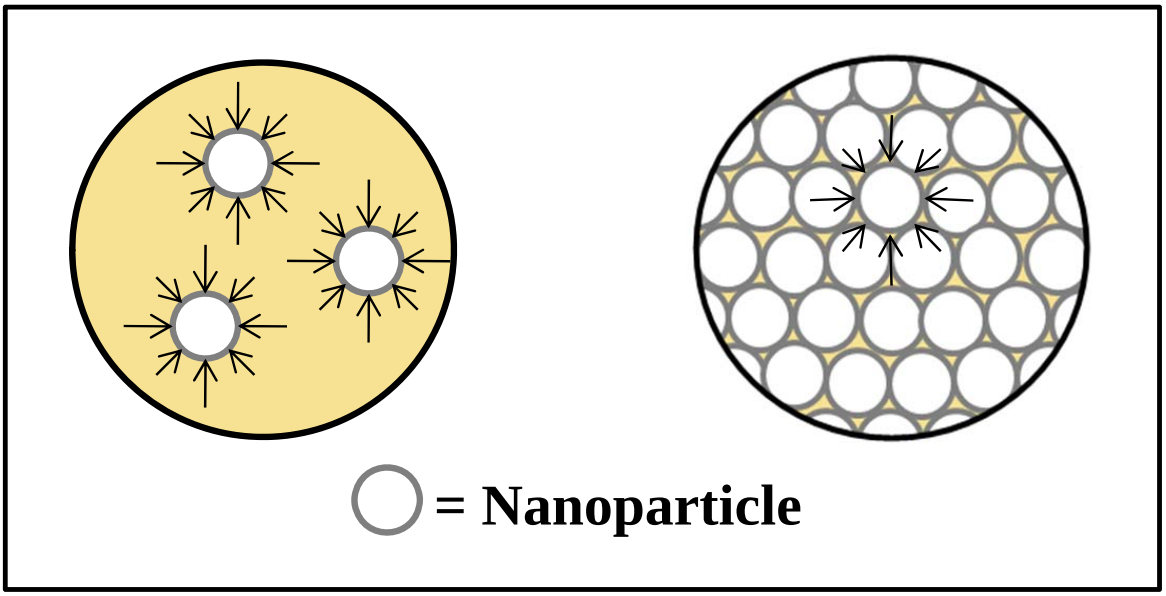

Figure 3.1: Increased load carrying capability with particle-to-particle contact

Lower volume fraction samples are dominated by matrix-particle contact, where the less stiff polymer matrix deforms around the particle. For higher volume fraction samples, as shown by the extreme representation in Figure 3.1, individual particles touch neighboring particles resulting in a significant increase in the load carrying capability of

the mixture [18] due to increased stiffness of the particles. However, in order to maximize the benefit of particle modifiers in a matrix on the mechanical properties, relatively uniform particle dispersion must be achieved to ensure an even stress distribution through the sample.

3.1.3 Aspect Ratio

Aspect ratio plays an important role on the mechanical response of samples. Edge effects caused by friction between the sample surface and loading platens can cause stress concentrations at each loading interface. If the aspect ratio is too small, these stress concentrations can cause higher stresses in the mid-region of the sample, which could lead to premature failure. If the aspect ratio is too large, buckling can occur under compression, leading to premature sample failure.

In this work, a length to diameter aspect ratio of 2:1 was maintained, as this ratio is generally accepted for quasi-static compression testing [41]. Under these conditions, the mechanical response can be optimized by avoiding frictional edge effects and minimizing the chance of sample buckling.

3.2 Fabrication of Alumina-Epoxy Composites

3.2.1 Bulk Composite Manufacturing

For low strain rate measurements, the bulk alumina-epoxy composite must first be fabricated. This fabrication procedure closely followed the procedure from earlier work [75]. In order to fabricate the bulk alumina-epoxy composites, α-alumina nanopowder with an average particle size of 150 nm, 99.85% purity, and a density of 3.97 g/cm^3 was used as the filler material. The epoxy resin, density of 1.17 g/cm^3, and curing agent implemented was Epon 862 (Bisphenol-F type) and Epikure-W, respectively. Volume fractions were chosen to correlate to static studies [75], which resulted in 4.5, 13.6, and 29.7% alumina filler material. It has been shown that 43% α-alumina is the maximum amount that can be added to an epoxy without reducing the overall mechanical properties of the epoxy itself [61]. The manufacturing process is shown in Figure 3.2.

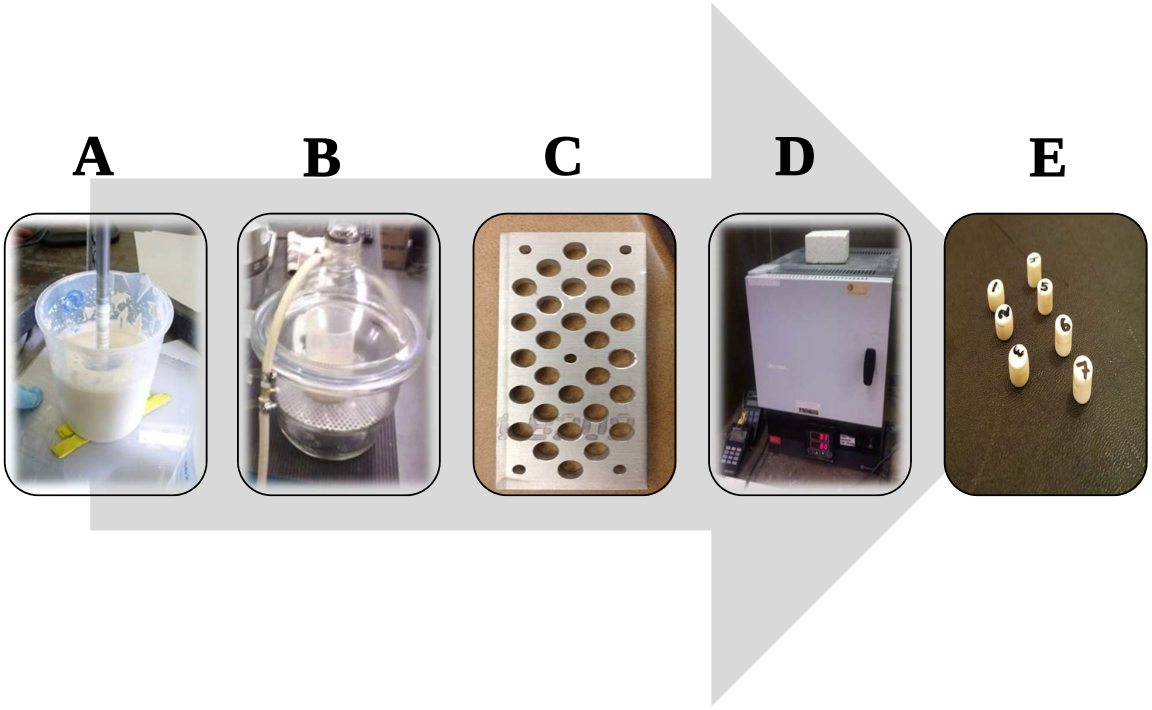

Figure 3.2: Fabrication of alumina-epoxy composites to include A) shear mixing, B) degassing, C) casting, D) curing, and E) sample removal

The appropriate amounts of each component, α-alumina nanoparticles and epoxy resin were measured and mixed using a high shear mixer for a duration of 1 hour. The curing agent was measured and added to the particle-epoxy mixture and mixed for an additional hour. The use of a high shear mixture removed most of the agglomerates that were present, and a low-pressure vacuum system was then utilized for approximately 1 hour to completely remove entrapped air bubbles. The mixture in its uncured state was transferred to a 0.5 *in* thick aluminum mold with 0.2 *in* diameter holes. As it is generally

accepted that quasi-static compression tests should have a length to diameter ratio of 2:1 [41], the mold thickness was kept slightly larger than the desired specimen length to allow for surface finishing of the top and bottom faces. The cast composite was cured for 4 hours in a furnace at 120°C. After the curing process was complete, the mold was removed from the furnace and the nanocomposite billets were removed while the mold was still warm using a gentle extraction process.

3.2.2 Surface Finishing

Upon complete cooling, the top and bottom faces of the cylindrical samples were surface finished to ensure parallelism. This was accomplished by the use of an aluminum jig with holes slightly larger than the sample diameter to ensure the samples fit securely as shown in Figure 3.3.

Figure 3.3: Surface finishing using an aluminum jig

Each sample was carely finished using a fine grit sanding process which included the use of varying degrees of grit to ensure a smooth top and bottom face. Finished sample dimensions were approximately 0.2 *in* diameter with 0.4 *in* length. Sample geometry was chosen based upon work by Lankford [46] and Jordan [41] to ensure right cylindrical samples with an aspect ratio of 2:1.

3.2.3 Strain Gage Attachment

In order to ensure superior attachment of the strain gage to the sample, the region of strain gage attachment for each sample was lightly sanded and the sample was extensively cleaned. Small tick marks were carefully drawn on the sample to ensure vertical and horizontal alignment of the gage to the sample as shown in Figure 3.4.

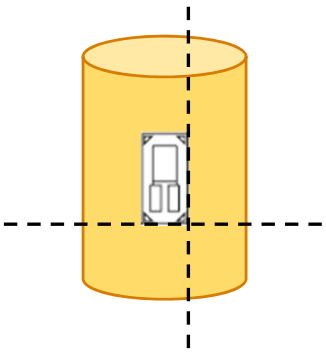

Figure 3.4: Strain gage attachment

Tape was used to align each annealed constantan foil gage with the tick marks, and the gage was subsequently attached with a fast-acting cyanoacrylate adhesive. After a 24 hour cure, the tape was removed and additional wire was soldered onto the beryllium Copper lead wires. Just before testing each sample, the strain gage was attached to a wheatstone quarter bridge setup as shown in Figure 4.1.

3.3 Material Property Determination

3.3.1 Intensity Measurements for Dispersion Verification using Photo-Stimulated Luminescence Spectroscopy

In order to ensure sufficient dispersion of the nanoparticles within the epoxy matrix, intensity measurements were collected using a spectrometer and coupled fiber optic probe. PSLS readings with an exposure time of 0.1 s and 1 accumulation for 4.5 and 29.7% and 0.05 s and 3 accumulations for 13.6% were collected using a five point scan along the length of the sample as shown in Figure 3.5.

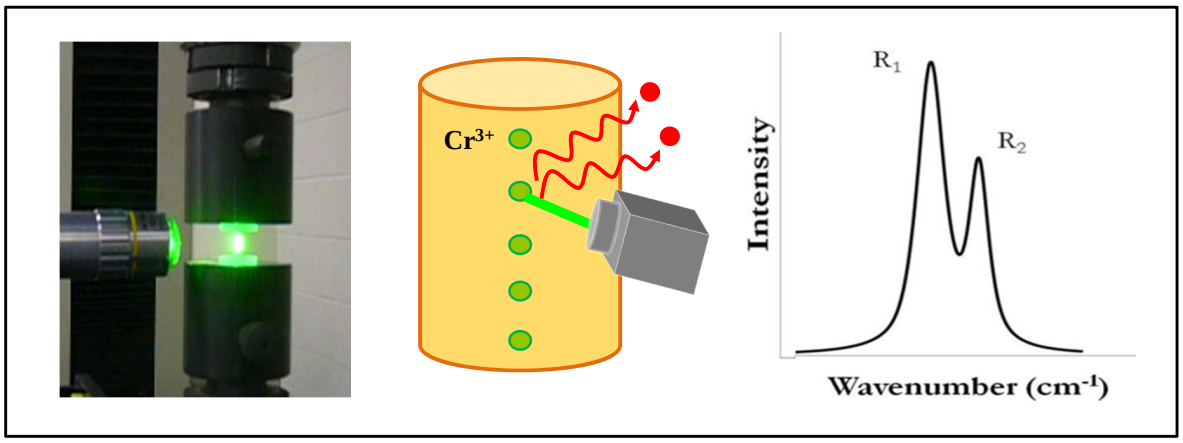

Figure 3.5: Data collection for dispersion verification

The exposure time for each volume fraction was determined in order to allow for sufficient exposure and resulting photo-luminescence, which is needed to produce sufficient intensities for monitoring. For each point, the data was deconvoluted as described in 2.2.1 and the intensity compared. Previous work with alumina-epoxy composites verified the ability to determine sample dispersion using the PSLS method [75]. The maximum and minimum intensity value for each sample was compared and dispersion was characterized as the variance of intensity on a local sample scale. The result for each sample is presented in Table 3.1.

Table 3.1: Intensity variance for each sample

Volume %	Sample ID	Intensity Variance %
4.5	1	7.71
	2	31.06
	3	9.48
	4	19.83
	5	11.05
	6	12.63
	7	4.18
	8	6.42
	9	4.64
13.6	1	3.36
	2	6.38
	3	12.72
29.7	1	19.42
	2	20.86
	3	27.40
	4	14.28
	5	19.17
	6	8.47
	7	15.08
	8	6.73

For 4.5% volume fraction samples, the intensity variance was determined to range between 4.18 and 31.06% with the average variance equal to 11.89%. Of the three volume fractions investigated, 13.6% revealed the lowest intensity variance average of 7.48% with values in the range of 3.36 to 12.72%. Recording the highest intensity variance average at 16.43%, the 29.7% volume fraction sample intensity variance ranged between 6.73 and 27.40%. Therefore, it can be concluded that the 13.6% volume fraction samples were generally more well dispersed, followed by 4.5 and 29.7%, with 29.7% generally having the poorest dispersion of all the volume fractions.

3.3.2 Density Measurements for Volume Fraction Verification

In order to calculate the actual volume fraction of the manufactured samples, density measurements were recorded. The following equations were used to determine the correct volume fraction of filler material:

$$\rho_{NC} = v_f \rho_f + v_m \rho_m \tag{3.1}$$

$$v_m = 1 - v_f \tag{3.2}$$

where ρ_{NC} is the measured density of the nanocomposite, v is the volume fraction, ρ is the known density for each material, and the subscripts f and m refer to the filler and matrix, respectively. Results for the volume fraction of both filler and matrix material are

shown in Table 3.2 along with the measured density of the nanocomposite. As expected, the measured densities of 1.30, 1.55, and 2.00 g/cm^3 yield increasing volume fractions of 4.5, 13.6, and 29.7%, respectively.

Table 3.2: Volume fraction and measured density of each volume fraction composite

Volume Percent of Filler	Volume Percent of Matrix	Density (g/cm^3)
4.5	95.5	1.30
13.6	86.4	1.55
29.7	70.3	2.00

3.3.3 Elastic Modulus Determination

The elastic modulus for composites can be determined by utilizing the theory of the rule of mixtures which defines the elastic modulus of a composite as:

$$E_{NC} = v_f E_f + v_m E_m \tag{3.3}$$

where E is the elastic modulus, v is the volume fraction, and the subscripts f and m refer to the filler and matrix respectively as shown in Table 3.3. As expected, the elastic modulus increases with increasing volume fractions reported as 15.80, 42.88, and 90.79 GPa for 4.5, 13.6, and 29.7% volume fractions, respectively.

Table 3.3: Elastic modulus (E_{NC}) of each volume fraction composite

Volume Percent of Filler	Volume Percent of Matrix	E_{NC} (GPa)
4.5	95.5	15.80
13.6	86.4	42.88
29.7	70.3	90.79

3.4 Experimental Setup

A Renishaw Raman spectrometer with a 2400 l/mm grating and attached fiber optic probe [23] was used to obtain PSLS readings. A Ne-Ar source was used to calibrate the spectrometer before data collection. The laser used had an excitation wavelength of 532 nm with approximately 18.5 mW of power at the probe exit. A MTS Insight Electromechanical system with a calibrated 10 kN load cell was utilized to apply a compressive stress via crosshead deflection. Lubricated sapphire platens were placed between the cylindrical samples and the MTS steel compression platens to reduce the effects of friction. The complete experimental setup is shown in Figure 3.6. This experimental setup was utilized for both mechanical and piezospectroscopic characterization.

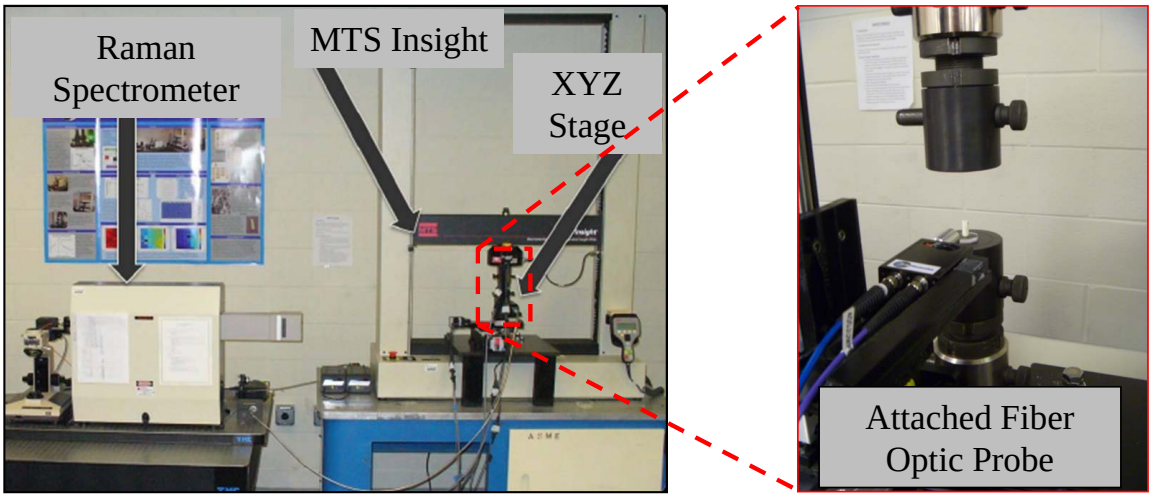

Figure 3.6: Experimental setup

CHAPTER 4
MECHANICAL ANALYSIS OF ALUMINA-EPOXY COMPOSITES UNDER QUASI-STATIC CONDITIONS

4.1 Objectives

Improved mechanical properties, such as toughness, corrosion resistance, and strength, have motivated the use of particulate composites in many applications. Alumina-epoxy composites are no exception and have often been utilized due to high particle stiffness and improved mechanical properties of interest. With the increased use of alumina particulate composites, comes the need to understand the material behavior under various loading conditions, whether static, quasi-static, or dynamic conditions exist.

In static studies on alumina-epoxy composites of varying volume fractions, mechanical strength was shown to improve with alumina content [75, 77]. On the other hand, several studies have reported the dynamic response of alumina-epoxy composites, where the mechanical strength was shown to improve with both increasing volume fractions of alumina and increasing strain rates [68, 61].

The test methods in this study utilize conventional strain gages to monitor the overall composite response including the linearity of strain behavior. However, the micromechanics, including particle interactions between the matrix and particles and interparticle effects, are not captured by strain gage measurements, which monitor the composite behavior on a macroscale. The collection of spectral emission using piezospectroscopy has

promise in terms of providing an insight on the particle-to-matrix behavior, which could substantially improve material strengthening mechanisms.

The strain gage studies performed here, in-situ with PS data collection, provide correlating behavior of the overall composite and the linear strain range for PS analysis.

4.2 Data Collection

A MTS Insight Electromechanical system was utilized to apply a stress via crosshead deflection in order to achieve target strain rates of 10^{-4}, 10^{-3}, and $10^{-2}s^{-1}$. The maximum force the sample sustained was recorded using values from the electromechanical test system. This value was divided by the initial sample cross-sectional area and correlated to calculated strain values using data from attached strain gages.

Strain gages made from annealed constantan foil with a tough, high-elongation polyimide backing, gage factor of approximately 2.05 - 2.1, Beryllium Copper lead wires, and a strain range of up to 20% were used to collect in-situ strain information with respect to time during loading. A schematic illustrating the strain gage connections is shown in Figure 4.1.

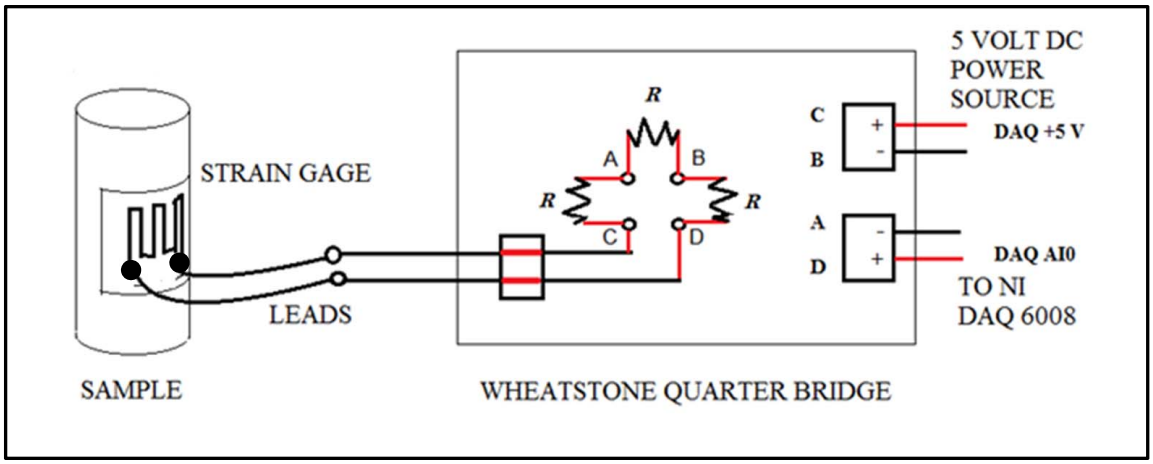

Figure 4.1: Strain gage setup

The strain gage lead wires were attached to a terminal block, connecting the strain gage across nodes CD as shown in Figure 4.1. A DC power source rated at 5V was connected across nodes CB in Figure 4.1, which was dissipated across the two resistors CA and AB in series, as well as the strain gage and resistor DB in series. Since the sample was loaded in compression, it was expected that the resistance on the gage would decrease, as well as the voltage across the gage, which would result in a slightly higher potential at node D than at node A as shown in Figure 4.1. By measuring the voltage difference across node DA with the NI DAQ 6008, as shown in Figure 4.1, it was possible to calculate the strain experienced by the gage.

4.3 Loading Rates

The calculated strain was plotted against time in order to elucidate the actual strain rate for each sample by analyzing the linear portion of data. In the event that strain information was unable to be recorded, strain rates were estimated using the parameters from the electromechanical test system. Loading rates for 4.5% as calculated from the strain gage data are shown in Figure 4.2. Sample 1 and Sample 8 for 4.5% have estimated strain rates of 10^{-4} and $10^{-2}s^{-1}$, respectively.

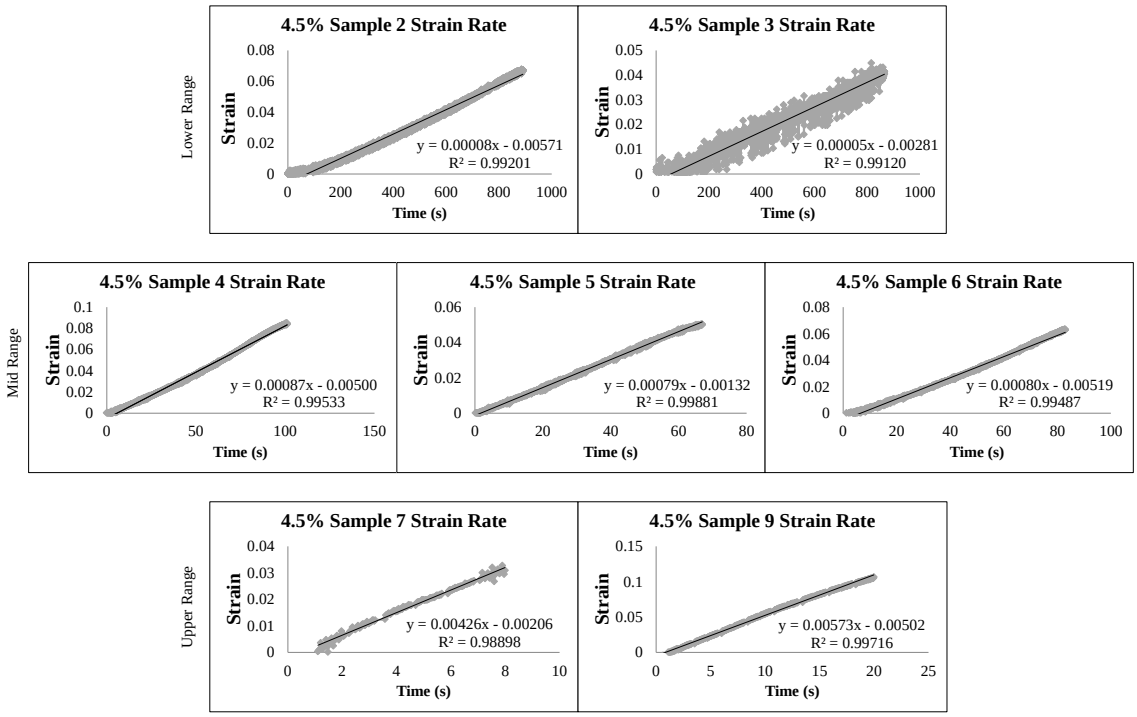

Figure 4.2: Strain rates as calculated from strain gage data for 4.5% volume fraction

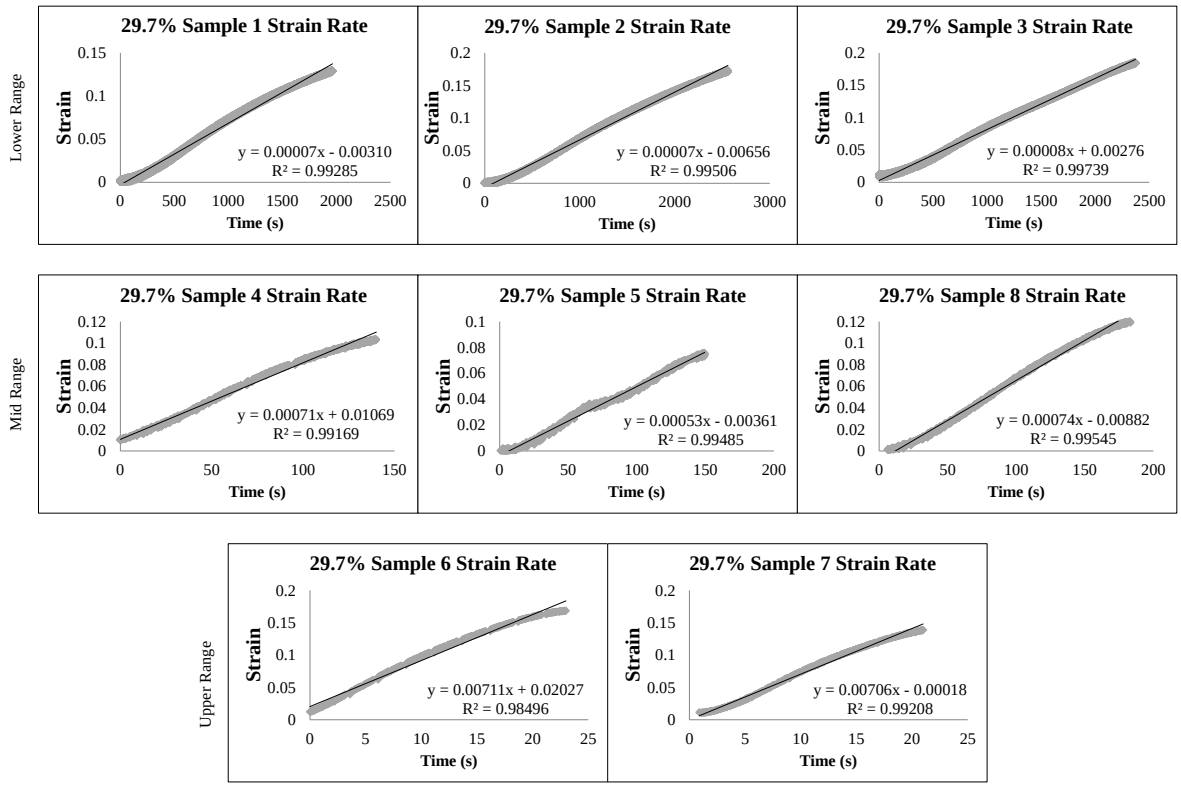

Figure 4.3: Strain rates as calculated from strain gage data for 29.7% volume fraction

Due to the absence of strain gages on all 13.6% samples, loading rates for 13.6% are estimated values and are 10^{-4}, 10^{-3}, and $10^{-2}s^{-1}$ for Sample 1, Sample 2, and Sample 3, respectively. Loading rates for 29.7% as calculated from the strain gage data are shown in Figure 4.3.

The loading rates for each sample are summarized in Table 4.1. Estimated strain rate values are indicated by an asterisk.

Table 4.1: Strain rate for each sample where * denotes an estimated value

Volume %	Sample ID	Strain Rate (s^{-1})
4.5	1	0.0001*
	2	0.00008
	3	0.00005
	4	0.00087
	5	0.00079
	6	0.00080
	7	0.00426
	8	0.01*
	9	0.00573
13.6	1	0.0001*
	2	0.001*
	3	0.01*
29.7	1	0.00008
	2	0.00008
	3	0.00008
	4	0.00071
	5	0.00053
	6	0.00711
	7	0.00706
	8	0.00074

4.4 Determination of the Mechanical Performance Dependency on Strain Rate

4.4.1 4.5% Volume Fraction Alumina-Epoxy Composites

Using the strain rates as defined in Table 4.1, ultimate strength dependence on strain rate was plotted for 4.5% as shown in Figure 4.4. Results reveal a general trend of increasing ultimate strength with increasing strain rate. However, at strain rates in the range of $10^{-4}s^{-1}$, the lower range, a slight trend of decreasing ultimate strength with strain rate is revealed, which could be attributed to the normal variance of experimental data due to sample defects. Additionally, data points at 10^{-4} and $10^{-2}s^{-1}$ are estimated strain rates, therefore, some error exists between this estimated value and calculated values from strain gage measurements.

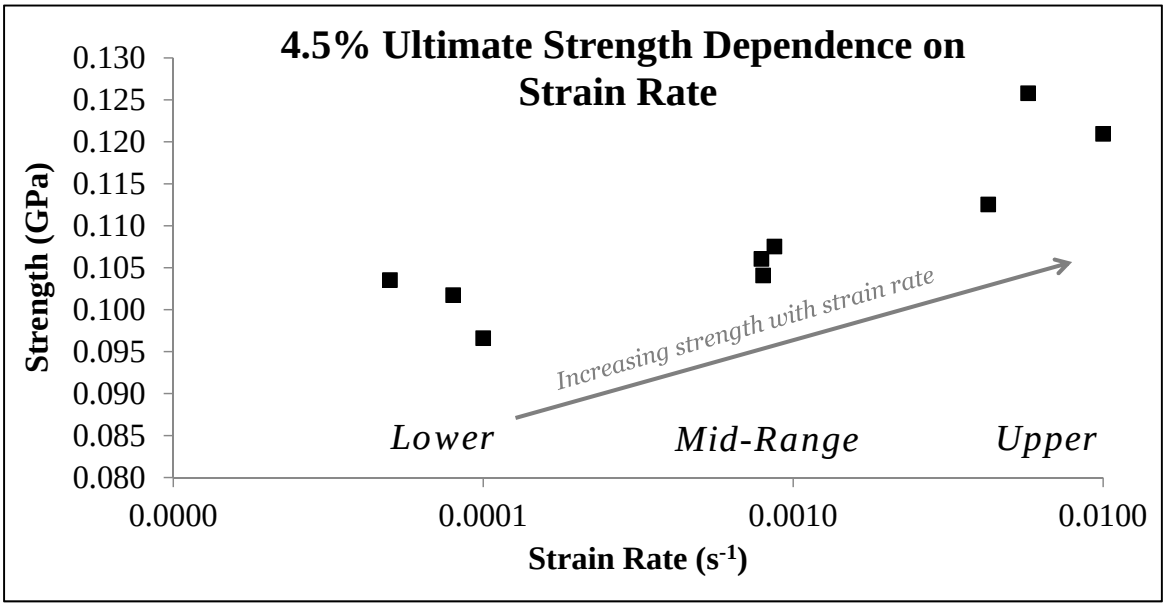

Figure 4.4: Ultimate strength dependence on strain rate for 4.5% volume fraction

4.4.2 13.6% Volume Fraction Alumina-Epoxy Composites

In a similar manner, the ultimate strength dependence on strain rate was plotted for 13.6% as shown in Figure 4.5 by using the estimated strain rates as defined in Table 4.1. Results reveal a general trend of increasing ultimate strength with increasing strain rate through the lower, mid, and upper ranges. However, each of these data points are estimated strain rates, therefore, some error exists between this estimated value and calculated values from strain gage measurements.

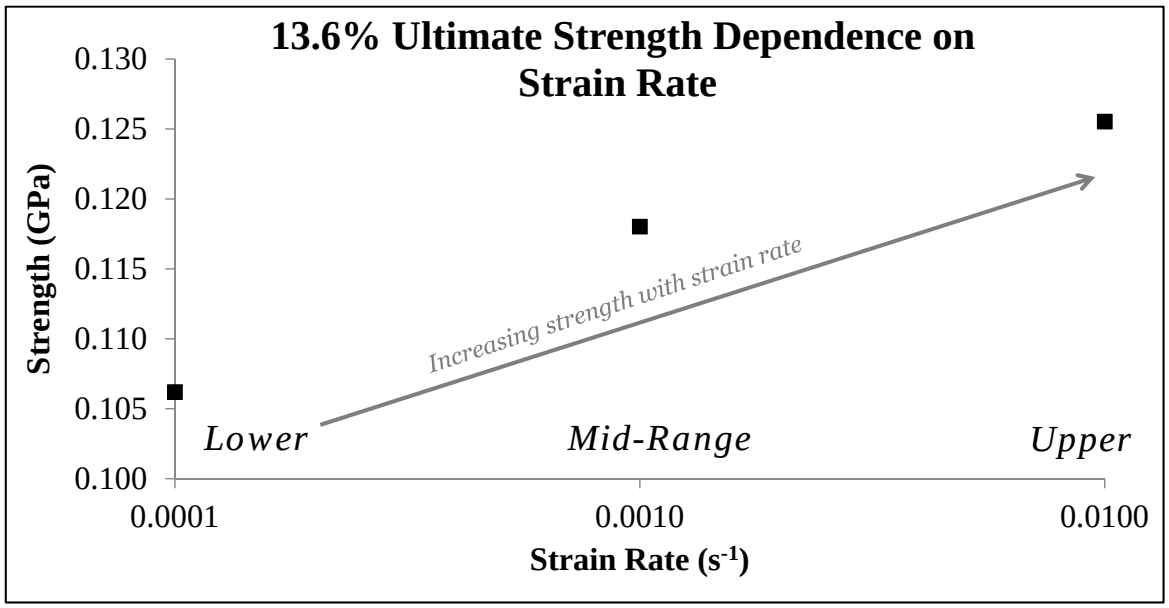

Figure 4.5: Ultimate strength dependence on strain rate for 13.6% volume fraction

4.4.3 29.7% Volume Fraction Alumina-Epoxy Composites

Using the strain rates as defined in Table 4.1, ultimate strength dependence on strain rate was plotted for 29.7% as shown in Figure 4.6. Results reveal a general trend of increasing ultimate strength with increasing strain rate at strain rates in the mid-range of $10^{-3}s^{-1}$. However, at strain rates in the lower range of $10^{-4}s^{-1}$, ultimate strength varies significantly with little change in strain rate. Similarly, results in the upper range of $10^{-2}s^{-1}$ show variation in the ultimate strength with little change in strain rate. Since 29.7% volume fraction samples are fairly difficult to manufacture and dispersing

the alumina particles evenly within the matrix proves challenging, these fluctuations in ultimate strength could be attributed to uneven particle dispersion or sample defects, such as agglomerations or voids.

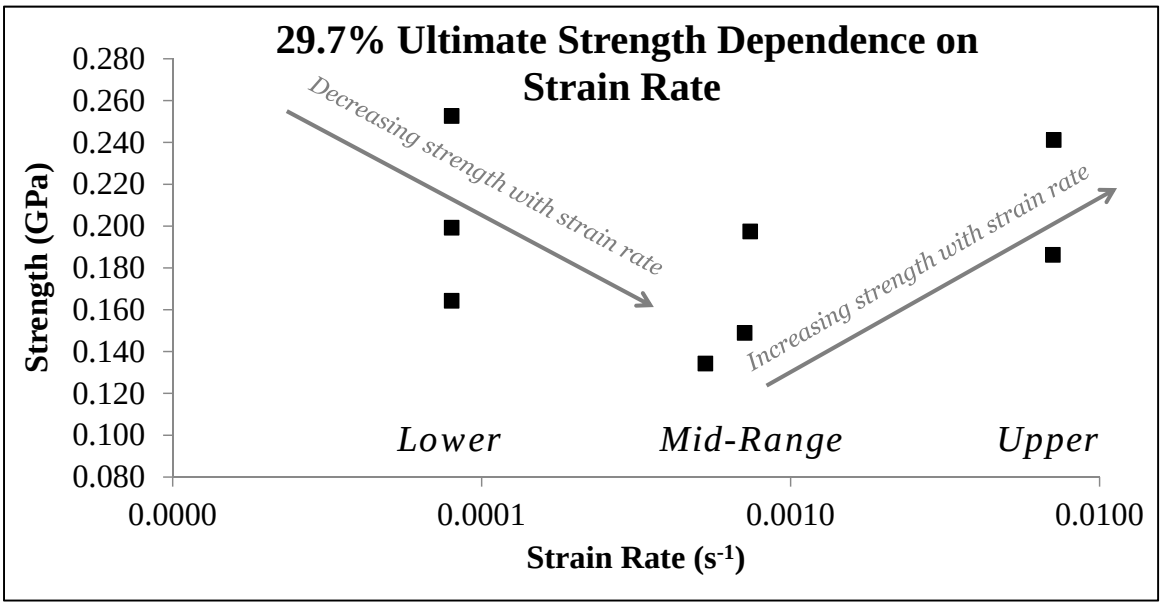

Figure 4.6: Ultimate strength dependence on strain rate for 29.7% volume fraction

4.4.4 Combined Mechanical Results

In order to determine the effect of volume fraction on the ultimate strength dependence with strain rate, 4.5, 13.6, and 29.7% volume fractions were plotted as shown in Figure 4.7 using the strain rates as defined in Table 4.1. Results reveal a general trend of increasing ultimate strength with increasing volume fraction for all three strain rate ranges of 10^{-4}

(lower), 10^{-3} (mid), and $10^{-2}s^{-1}$ (upper). In each range, 4.5 and 13.6% volume fractions show little variation in strength values, however, 29.7% shows a substaintal increase in ultimate strength over 4.5 and 13.6%. This mechanical response is expected, as adding nanoparticle modifers to a weaker epoxy matrix, generally increases the strength of the composite.

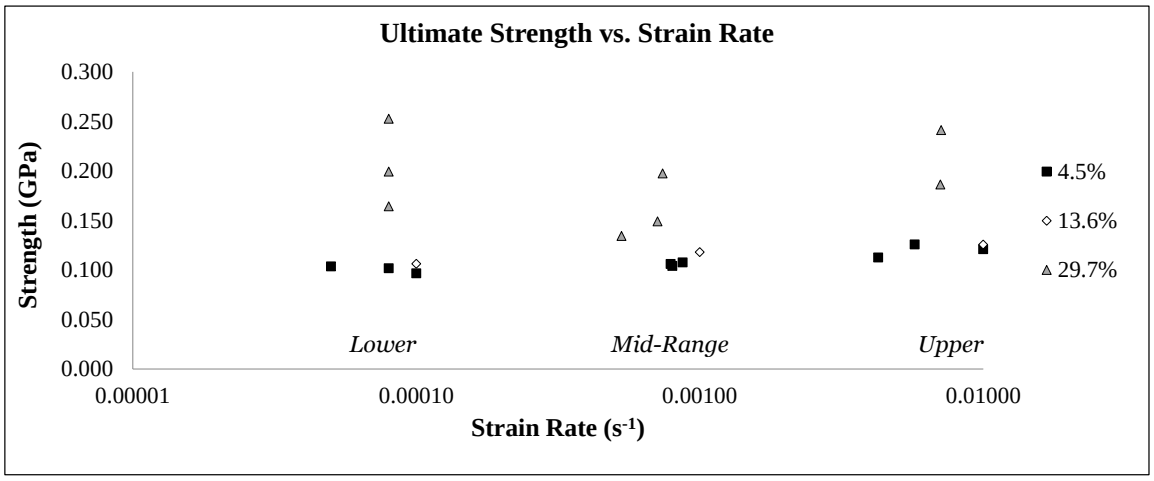

Figure 4.7: Ultimate strength dependence on strain rate for all volume fractions

4.5 Conclusion

The mechanical response of alumina-epoxy composites under quasi-static strain rates was investigated to determine the impact of strain rate on mechanical strength of the overall composite using conventional test methods. For 4.5 and 13.6% volume fraction

samples, a general trend of increasing ultimate strength with strain rate was revealed, as in generally expected for these materials, however, a trend was not as easily characterized with 29.7%. Results were also used to determine the linear range of strain, which was used to determine the range of stress for PS analysis as described in Section 5.3.

CHAPTER 5
PIEZOSPECTROSCOPIC ANALYSIS OF ALUMINA-EPOXY COMPOSITES UNDER QUASI-STATIC CONDITIONS

5.1 Objectives

As the Cr^{3+} ions within alumina are excited by a laser, photons are emitted at set wavelengths, which form the characteristic R-lines. Deformation to the particles due to an applied stress, causes the photons to emit at different wavelengths, which ultimately causes a shift in the characteristic R-lines. In relation to a reference position, typically an unstressed state, the peak position shift of the R-lines, to include R1 and R2, with applied load can be quantified and described by the PS effect.

In this work, the PS effect was investigated by monitoring the peak position shifts of R1 and R2 under dynamic loads to determine the PS coefficient for each sample, which is the slope of linear trend of the peak position shift with stress. In order to determine PS coefficients for 4.5, 13.6, and 29.7% volume fraction of alumina nanoparticles in an epoxy matrix under variable rates of loading, it is necessary to investigate these materials by utilizing their photo-luminescent properties. Each volume fraction should have sufficient intensity in regards to collection time in order to determine the R-line shifts with stress with precision without limiting the number of data collection points or causing camera saturation. By maximizing this combination, the photo-luminescent properties are able to be utilized to correlate the peak position shifts with stress. As a result, a PS coefficient

can be determined for each sample, which represents the amount of shift in wave number per unit of applied stress (cm^{-1}/GPa) to the nanocomposite.

Since the peak position shifts occur due to stresses experienced by the α-alumina particles, particles experiencing higher stresses, caused by external loading, will exhibit greater R-line peak position shifts. The PS coefficient, which relates the amount of applied stress to a measurable shift in peak position of the emission lines of embedded α-alumina particles, can ultimately be used as an indicator of load transfer to particles. Higher magnitude PS coefficients would relate to greater shifts, thus inherently more particle stress, for a range of applied loads than lower magnitude PS coefficients.

Static experimental test results on alumina-epoxy composites revealed increased PS sensitivity with increasing volume fractions for both R1 and R2 as a higher portion of the applied stress to the nanocomposite is supported by the much stiffer and stronger α-alumina nanoparticles [75]. However, that may not be the case for alumina-epoxy composites under quasi-static conditions, as time-dependent loading, stress transfer, and failure are much more complicated processes. Specifically, as the composite is loaded, the particles are initially confined by the weaker, less stiff epoxy matrix, which inherently transfers stress to the particles. However, as the loading process continues, particle-to-matrix contact transforms into particle-to-particle contact, which ultimately affects the load transfer mechanics and thus, resulting PS sensitivity. Eventually, the composite is limited by the strength of the epoxy matrix, and the composite fails due to microcracks that form within regions of high stress concentrations.

Additionally, with increasing concentrations of ceramic alumina nanoparticles to an epoxy matrix, the material has the tendency to become more brittle and the response more suseptible to changes in loading rate. Therefore, the R1 and R2 PS behavior for each volume fraction was investigated in the linear elastic region as determined through the mechanical analysis described in Section 5.3 and the results compared in order to determine composite sensitivity in regards to volume fraction and strain rate.

5.2 Data Collection

The spectrometer and coupled fiber optic probe, as shown in the experimental setup in Figure 3.6, were used to obtain PSLS readings with an exposure time of 0.1 s and 1 accumulation for 4.5 and 29.7% and 0.05 s and 3 accumulations for 13.6% at all rates of loading. The exposure time for each volume fraction was determined in order to allow for sufficient exposure and resulting photo-luminescence, which is needed for sufficient intensities to enable accuracy in R-line peak monitoring, without camera saturation. In the case of 13.6%, 3 accumulations were observed to limit the number of data collection points, especially at higher loading rates. Therefore, only 1 accumulation and sufficient exposure time was utilized for subsequent tests of 4.5 and 29.7% volume fractions at all loading rates.

The unloaded R-line peak positions for each sample were used as the reference point to which all subsequent R1 and R2 shifts with stress were analyzed. This reference position

would also account for any residual stress introduced by the manufacturing process and as a result, the PS coefficients presented in this work are determined with respect to the unloaded sample. Each sample was loaded continuously under compression at the quasi-static strain rates shown in Table 4.1 as determined by the attached strain gage. Photo-luminescent data was collected in-situ as shown in Figure 5.1 and peak position shifts for R1 and R2 were analyzed throughout the linear elastic region as discussed in the next section.

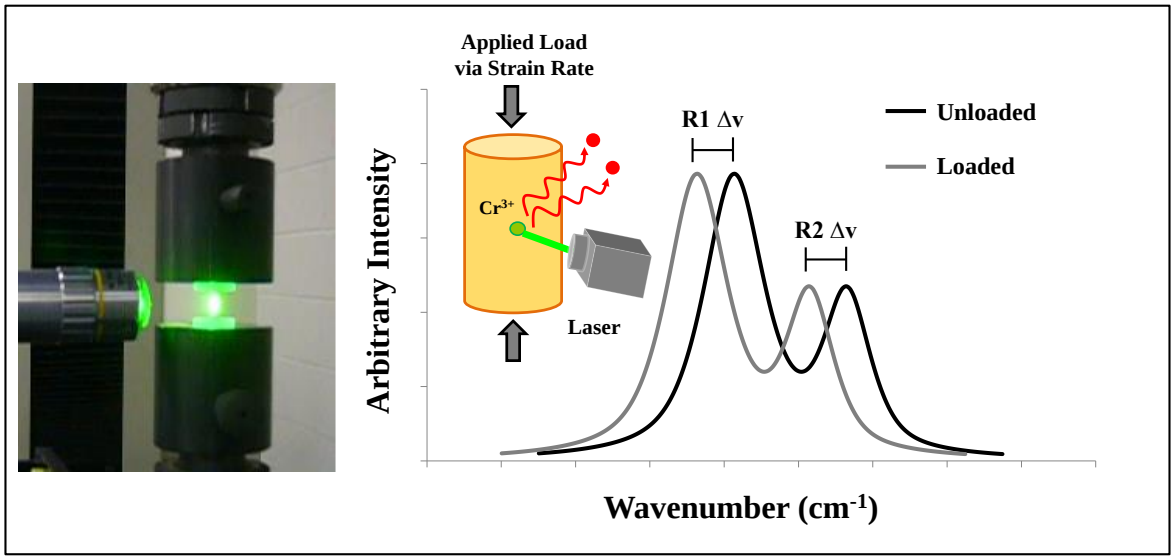

Figure 5.1: In-situ data collection for PS coefficient determination

The calculated PS coefficient as described in Equation 2.7 characterizes a linear trend which relates an applied stress to the nanocomposite to a shift in the captured photo-

luminescent R-lines, thus, ultimately describing the load transfer to the nanoparticles, serving as a mechanism to elucidate the load transfer sensitivity.

5.3 Correlation of Piezospectroscopic Findings with Mechanical Results

Due to the complex nature of time-dependent characterization and necessity to determine the PS relationship under linear elastic conditions, only the linear elastic region of the stress-strain response as established by the attached strain gage was used to correlate peak shift with stress. An example of the method used to find this region is shown in Figure 5.2. For samples with corresponding strain gage information, the maximum PS stress was determined in the manner shown in Figure 5.2, otherwise, it was estimated using the parameters from the electromechanical test system.

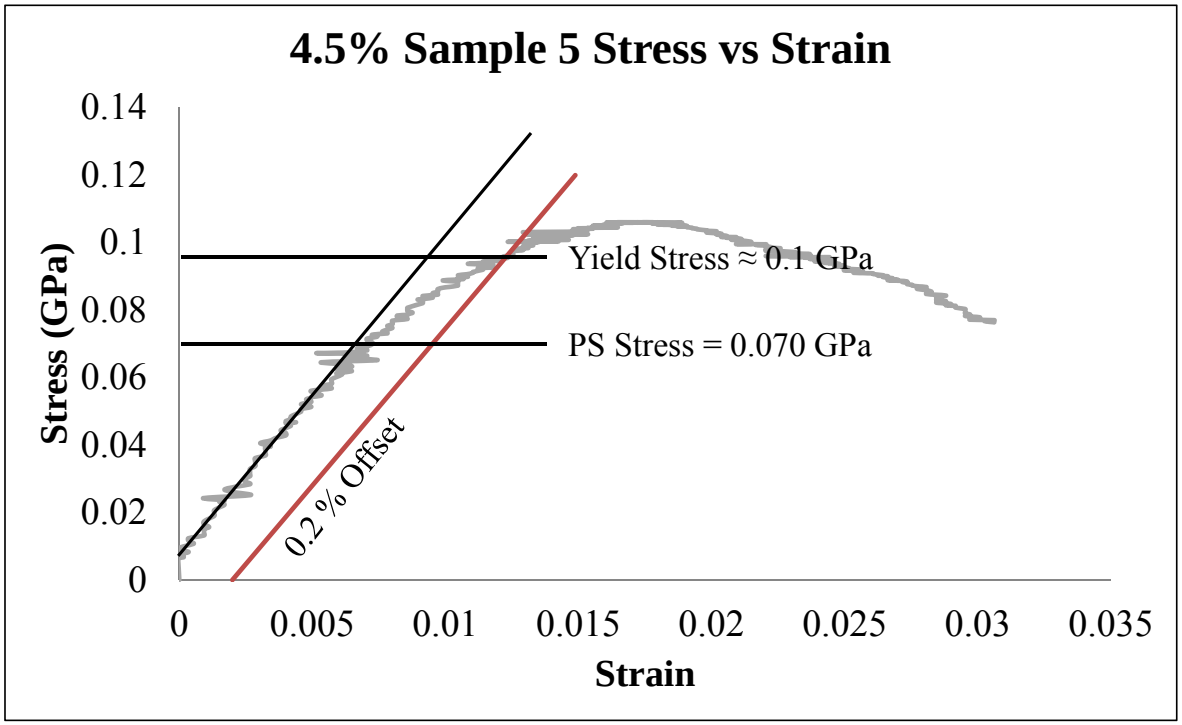

Figure 5.2: Method employed to calculate the linear range for PS coefficient analysis

The maximum PS stress values are different than the offset yield stress in order to determine the compressive PS coefficient with successive peak position downshifts exclusive of slight peak position upshifts. In this work, PS upshifts were noted to occur slightly before the offset yield stress, which may be the onset of microcracking and stress relief to the particles. Generally, the maximum PS stress values were approximately 70% of the offset yield stress. As a result, the maximum PS stress limits the region of PS analysis to correspond with stress-strain linearity and does not include regions of upshift, which would affect the sensitivity value. The maximum PS stress for all the

samples tested is shown in Table 5.1. Using this region of stress, the corresponding peak shift at a given applied stress for each sample was determined as outlined in the next section.

Table 5.1: Maximum PS stress for all samples

Volume %	Sample ID	Strain Rate (s^{-1})	Max PS Stress (GPa)
4.5	1	0.0001*	0.044
	2	0.00008	0.047
	3	0.00005	0.047
	4	0.00087	0.069
	5	0.00079	0.070
	6	0.00080	0.068
	7	0.00426	0.045
	8	0.01*	0.044
	9	0.00573	0.067
13.6	1	0.0001*	0.049
	2	0.001*	0.041
	3	0.01*	0.077
29.7	1	0.00008	0.089
	2	0.00008	0.099
	3	0.00008	0.095
	4	0.00071	0.088
	5	0.00053	0.084
	6	0.00711	0.099
	7	0.00706	0.059
	8	0.00074	0.093

5.4 Determination of the Piezospectroscopic Coefficient Dependency on Strain Rate

5.4.1 4.5% Volume Fraction Alumina-Epoxy Composites

Using the stress from the linear elastic region as defined in the previous discussion, the R1 and R2 peak shift with stress for each 4.5% volume fraction sample was analyzed as shown in Figure 5.3 and 5.4, respectively.

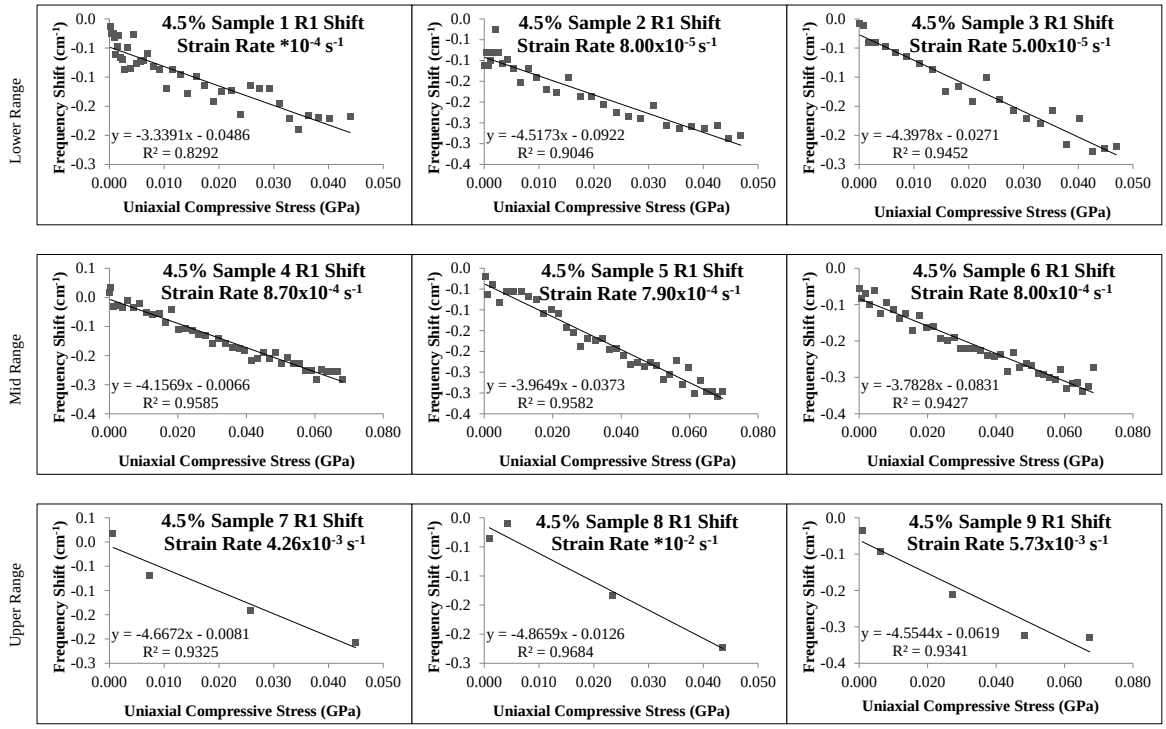

Figure 5.3: R1 peak position shift with stress for 4.5% volume fraction samples

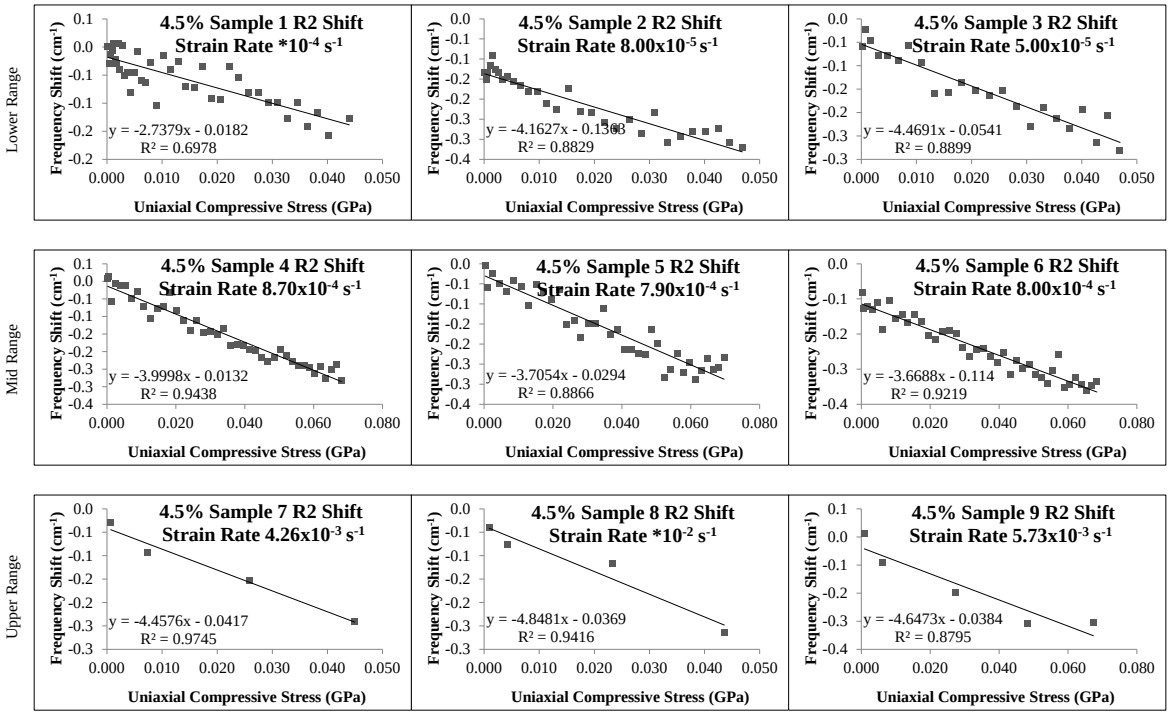

Figure 5.4: R2 Peak position shift with stress for 4.5% volume fraction samples

The capability to track changes in nanoparticle stress, i.e. load transfer, was verified by the ability to discern peak shifts for R1 and R2 even at relatively low stresses. Based on static results [75], which revealed increasing PS sensitivity with increasing volume fraction, tracking discernable peak shifts for 4.5%, even at low stresses, shows promise for continuous rate loading and collection.

As a means to quantify the R1 and R2 PS sensitivity with strain rate, the linear trend in peak position shift with stress was determined. Results for peak shift reveal goodness of fit values in the range of 0.83 to 0.97 for R1 and 0.70 to 0.97 for R2, thus,

lending confidence to the results. The slopes of the linear trend, the PS coefficients, range from -3.34 to -4.87 cm^{-1}/GPa for R1 and -2.74 to -4.85 cm^{-1}/GPa for R2. These results correlate well with the static data for 5% alumina, -3.16 cm^{-1}/GPa for R1 and -2.6 cm^{-1}/GPa for R2 [75]. Based on previous work with alumina-epoxy composites under static conditions where the PS coefficient was determined to increase with volume fraction, a composite with 4.5% volume fraction of particles would be expected to have a lower magnitude PS coefficient than a composite with 5% volume fraction of particles. Thus, the 4.5% volume fraction samples tested in this work, generally show increased PS sensitivity.

In order to determine the effect of strain rate on the PS coefficient sensitivity for 4.5%, the R1 and R2 PS coefficients for all samples were plotted against their respective strain rates as shown in Figure 5.5. A general trend of increased R1 and R2 PS coefficients for quasi-static strain rates over static values is revealed. However, a slight decrease in sensitivity is revealed between the lower and mid-range of strain rates tested, while an increase is revealed between the mid and upper range. Since the PS coefficient is akin to the load transfer to the nanoparticles, it is observed that the nanoparticles experience more stress at increased strain rates, thus indicating improved load transfer. In most cases, the R2 PS coefficient magnitude is slightly less than the R1 PS coefficient magnitude, but many of the values are closely grouped, lending confidence to results.

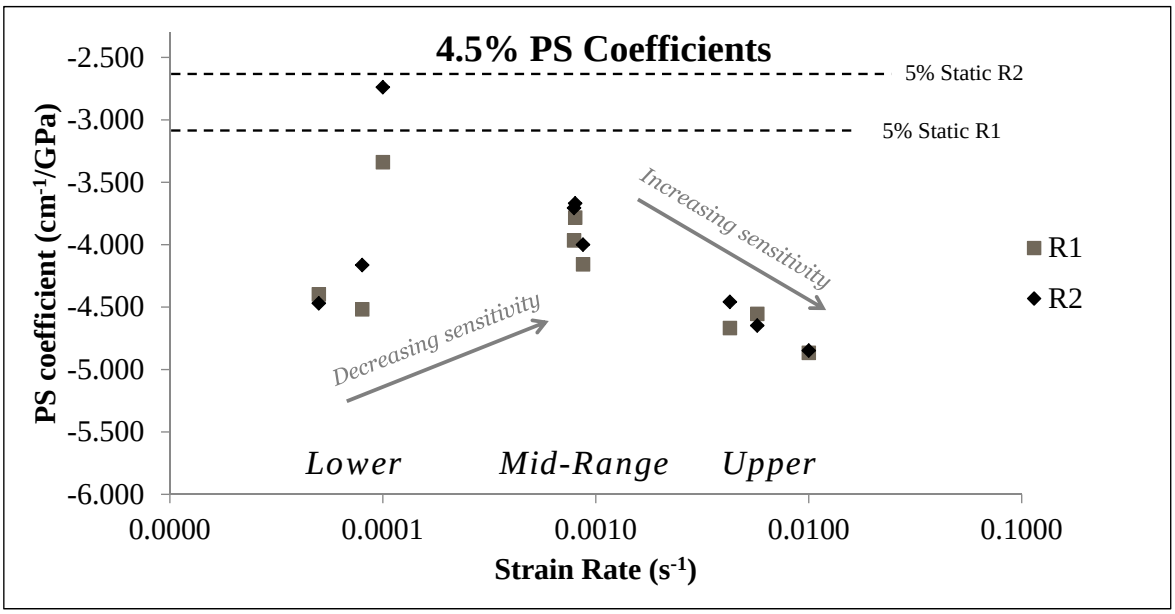

Figure 5.5: R1 and R2 PS dependence on strain rate for 4.5% volume fraction at quasi-static strain rates

5.4.2 13.6% Volume Fraction Alumina-Epoxy Composites

The R1 and R2 peak position shift with stress was analyzed for 13.6% using the estimated linear region as previously defined. Similarly to 4.5%, peak position shifts with stress were easily discernable for 13.6%, even at low stresses. Here again, the capability to track nanoparticle stresses and elucidate the load transfer at the nanoscale is verified by the ability to discern these shifts. As a means to quantify the PS sensitivity with strain rate,

the linear trend in peak position shift with stress was determined as shown in Figure 5.6 for R1 and Figure 5.7 for R2.

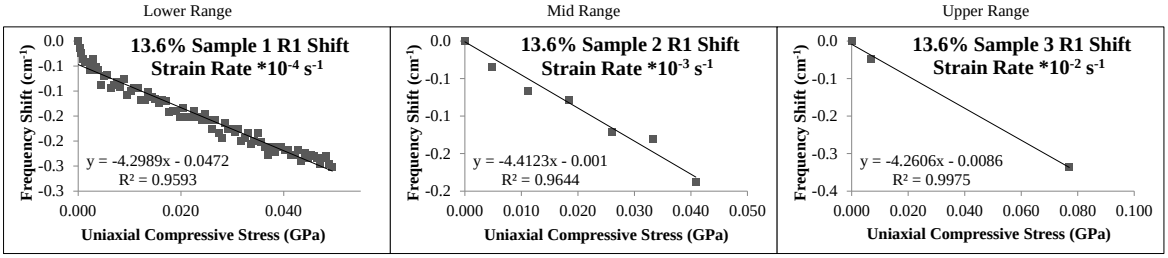

Figure 5.6: R1 Peak position shift with stress for 13.6% volume fraction

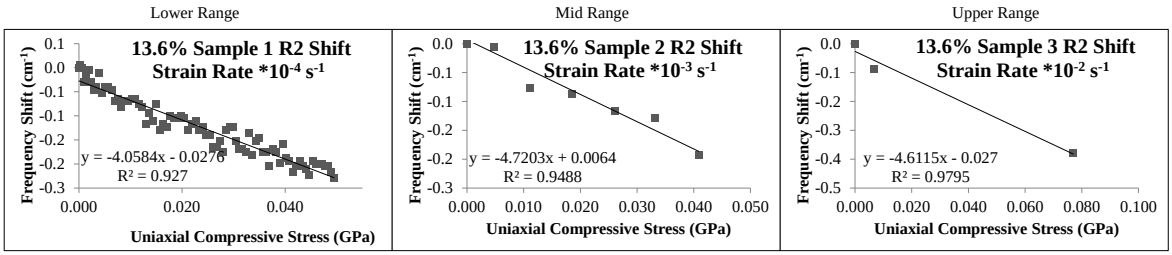

Figure 5.7: R2 Peak position shift with stress for 13.6% volume fraction

Results reveal goodness of fit values in the range of 0.96 to 0.98 for R1 and 0.93 to 0.98 for R2. R1 and R2 PS coefficients ranged from -4.26 to -4.41 cm^{-1}/GPa, and -4.06 to -4.72 cm^{-1}/GPa, respectively. While slightly higher in magnitude than the static value for 25% of -3.65 cm^{-1}/GPa [75], the PS coefficients for 13.6%, even considering

the lower volume fraction, have improved sensitivity to stress transfer under quasi-static conditions.

In order to determine the effect of strain rate on the PS coefficient sensitivity for 13.6%, the R1 and R2 PS coefficients for all samples were plotted against their respective estimated strain rates as shown in Figure 5.8. A general trend of increasing R1 and R2 PS coefficients is revealed between the lower and mid-range, while a slight decrease is evident in the mid to upper range. Actually, the R2 PS coefficients for the mid and upper range of strain rates showed more sensitivity to load transfer than in the lower strain rate region.

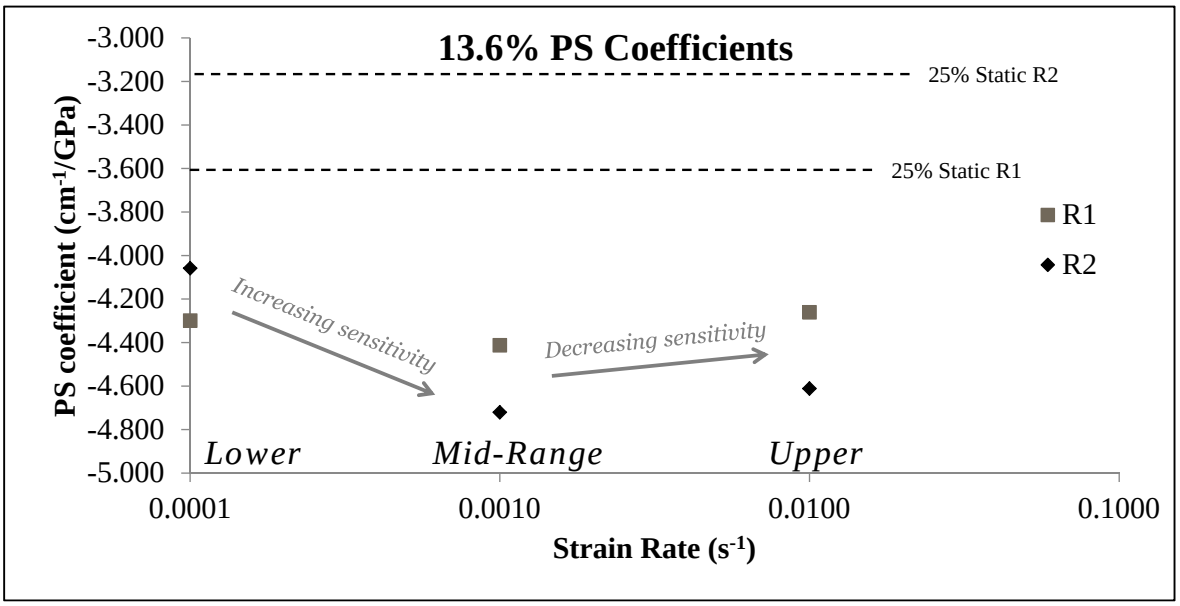

Figure 5.8: R1 and R2 PS dependence on strain rate for 13.6% volume fraction samples at quasi-static strain rates

5.4.3 29.7% Volume Fraction Alumina-Epoxy Composites

Using the stress from the linear elastic region as defined in previous discussion, the peak position shift with stress was plotted for each sample as shown in Figure 5.9 for R1 and Figure 5.10 for R2.

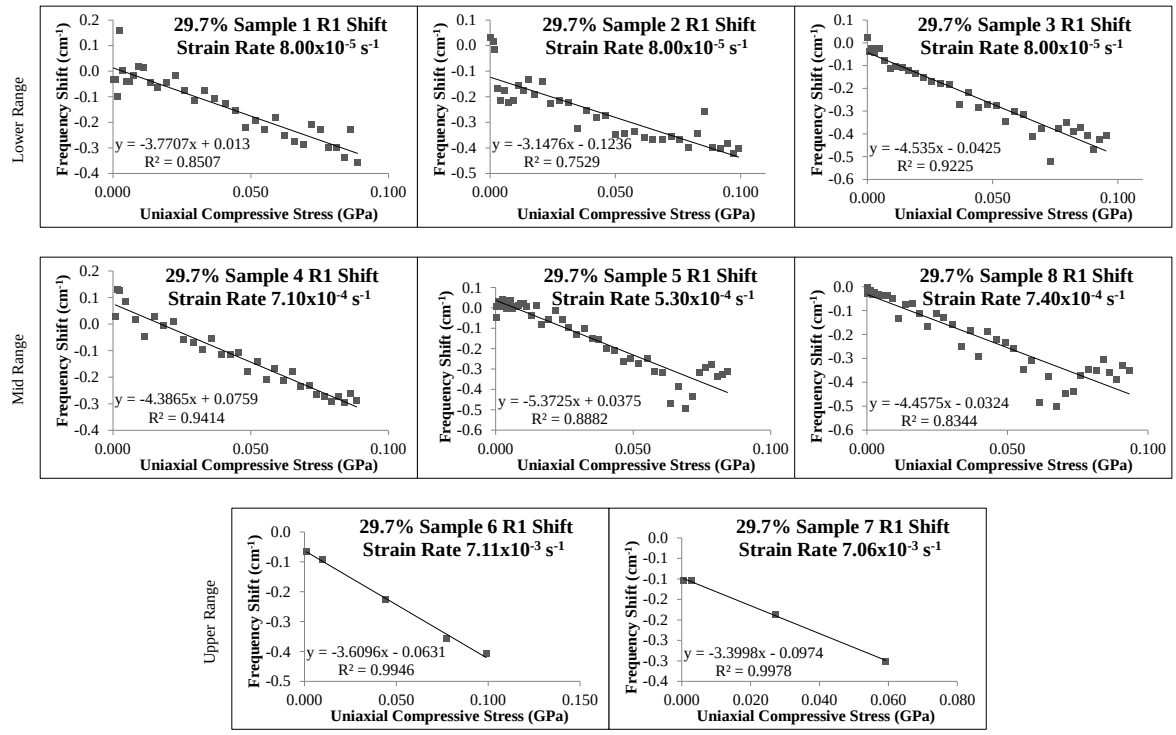

Figure 5.9: R1 Peak position shift with stress for 29.7% volume fraction

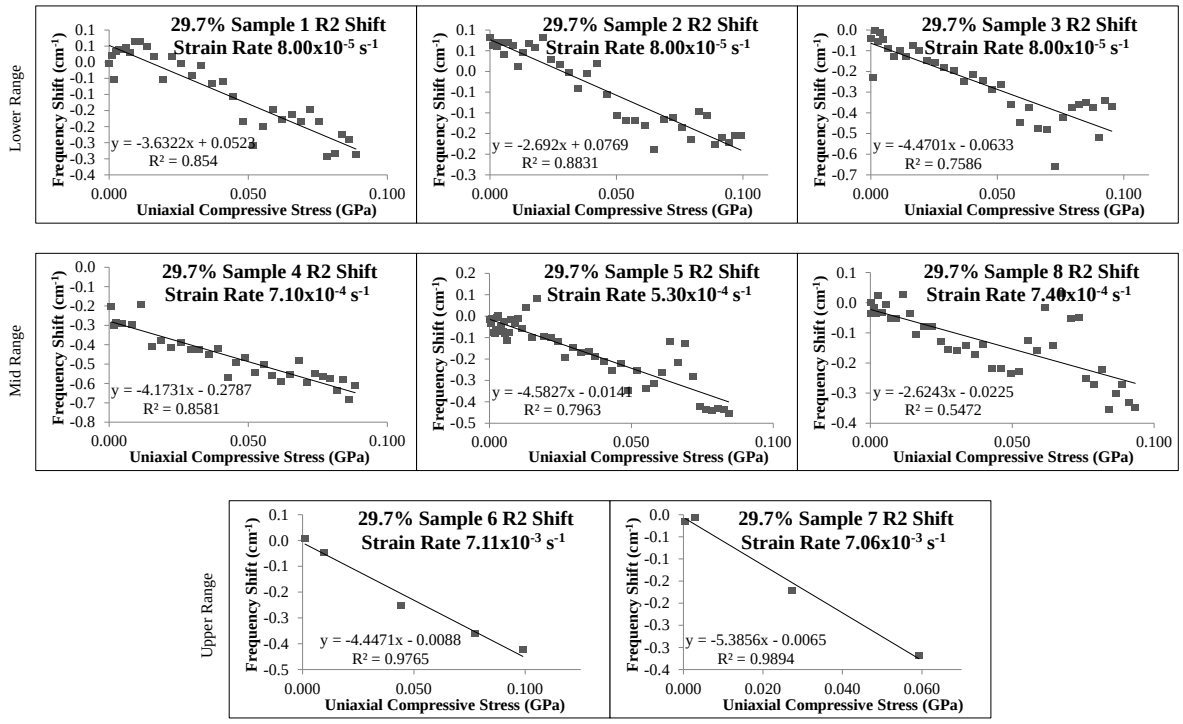

Figure 5.10: R2 Peak position shift with stress for 29.7% volume fraction

Results reveal goodness of fit values in the range of 0.75 to 0.99 for R1 and 0.55 to 0.99 for R2. R1 and R2 PS coefficients range from -3.15 to -5.37 cm^{-1}/GPa and -2.62 to -5.39 cm^{-1}/GPa, respectively. The R1 PS coefficient for sample 5, -5.37 cm^{-1}/GPa, was in the range of the 38% static value of -5.63 cm^{-1}/GPa for R1 [75]. On the other hand, the R2 PS coefficient for sample 7, -5.39 cm^{-1}/GPa, was in the range of the 38% static value of -5.08 cm^{-1}/GPa for R2 [75]. However, the magnitude of the R1 and R2 PS coefficients reported for the other 29.7% samples tested in this work are lower than the reported static values of -5.63 cm^{-1}/GPa for R1 and -5.08 cm^{-1}/GPa for R2 for 38%.

Due to the lower volume fraction of 29.7%, in comparison to 38%, lower PS coefficients are expected based on results of static work.

Higher volume fractions of alumina are notoriously more difficult to disperse within the matrix, which may lead to a higher prevalence of agglomerations, voids, or flaws within the sample. These material defects would ultimately change the way stress is distributed throughout the sample, attributing to poor load transfer and sensitivity. Additionally, higher volume fractions of alumina-epoxy composites behave differently than lower volume fractions due to the reduction in the amount of matrix binder and increased ceramic content, which may also change the stress distributions throughout the sample. This may help to explain the range of PS coefficients for the 29.7% samples.

Despite the span in R1 and R2 PS coefficients among the 29.7% samples, the PS coefficient sensitivity dependency on strain rate is shown in Figure 5.11. A general trend for the R1 and R2 PS coefficients in relation to strain rate for 29.7% is not easily ascertained. Again, this could be potentially explained by the difficulty in sample preparation of higher volume fractions and high likelyhood of poor dispersion, to include voids and agglomerations. These types of defects would greatly impact the load transfer mechanics, especially at increased rates of loading. However, there are some noticeable trends at each strain rate region. In the lower to mid-range, R1 PS coefficients indicate a greater sensitivity to load transfer for R1 in comparison to R2 as the magnitude in values for the R1 PS coefficients are greater. Generally, there is an increase in sensitivity for both R1 and R2 in the lower to mid-range of strain rates. On the other hand, in the upper strain

rate region, the R2 PS coefficients reveal heightened sensitivity to load transfer over R1, and a general decrease in sensitivity for both R1 and R2 in the mid to upper range is revealed.

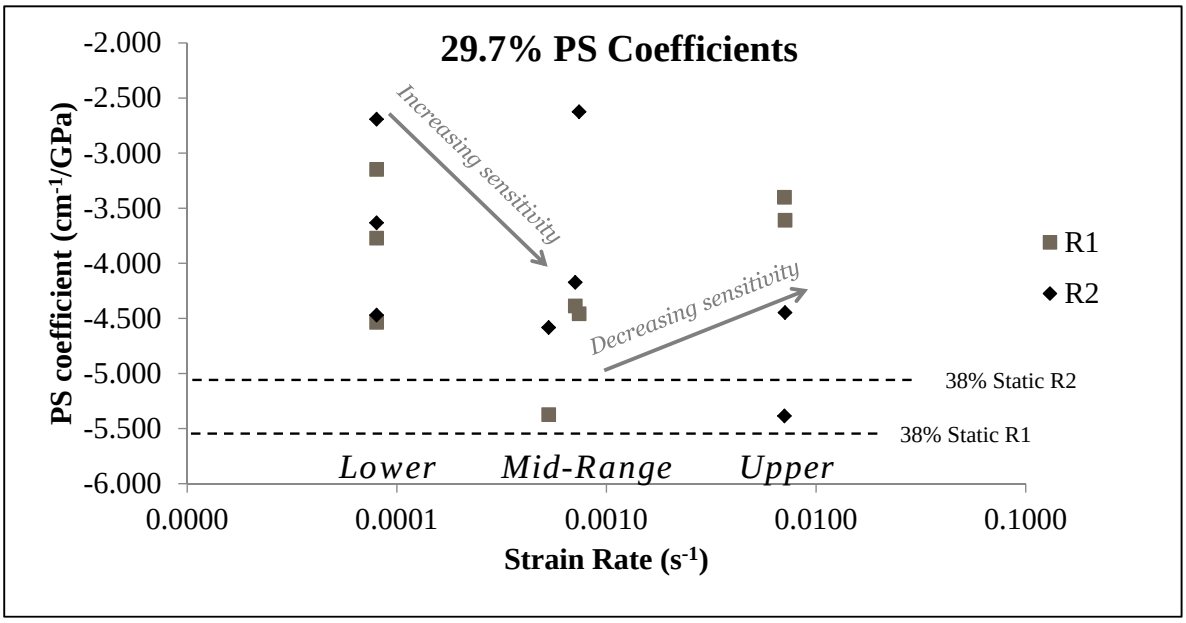

Figure 5.11: R1 and R2 PS dependence on strain rate for 29.7% volume fraction samples at quasi-static strain rates

5.4.4 Combined Piezospectroscopic Results

In addition to the effect of strain rate on the R1 and R2 PS sensitivity for the individual volume fractions, the PS coefficients for all volume fractions were plotted against strain

rate in order to determine the relationship between volume fraction, strain rate, and PS coefficient sensitivity. The R1 values are shown in Figure 5.12 and outlined in Table 5.2.

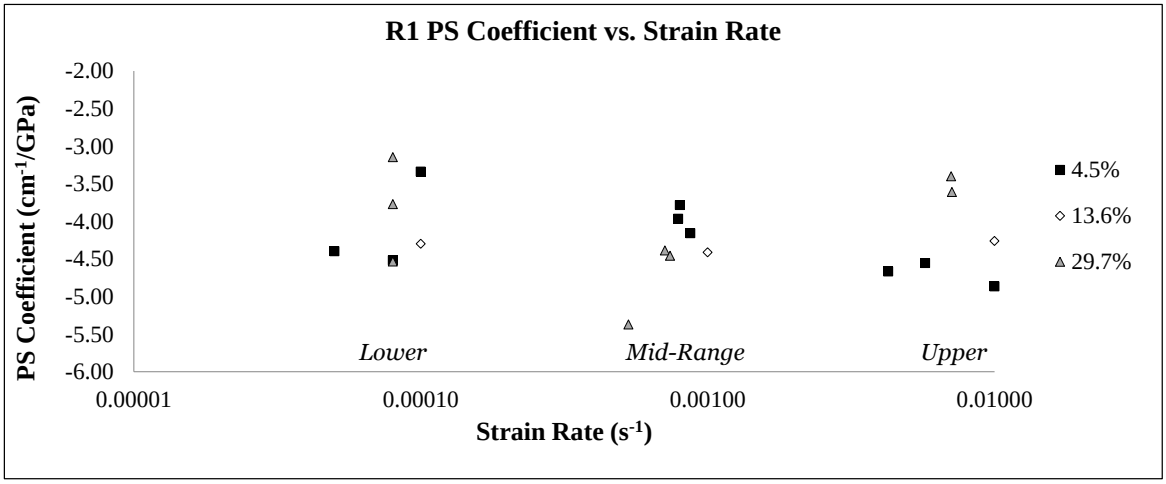

Figure 5.12: R1 PS coefficient dependence on strain rate for all volume fractions

As shown in Figure 5.12 for the lower range of strain rates around $10^{-4}s^{-1}$, R1 PS coefficients for 4.5, 13.6 and 29.7% vary in the range of -3 to -5 cm^{-1}/GPa with no clear determination of the effect of volume fraction on R1 PS coefficient sensitivity. In the mid-range of strain rates around $10^{-3}s^{-1}$, clear evidence of increasing R1 PS coefficient with increasing volume fraction is presented as 4.5% has the lowest magnitude R1 PS coefficients centralized around -4 cm^{-1}/GPa, 13.6% has a R1 PS coefficient at approximately -4.5 cm^{-1}/GPa, and 29.7% has the highest magnitude R1 PS coefficients between -4.5 and -5.50 cm^{-1}/GPa. In the upper range of strain rates around $10^{-2}s^{-1}$, R1 PS coefficients vary in the range of approximately -3.5 to -5 cm^{-1}/GPa with 4.5% volume

fraction exhibiting the highest sensitivity and 29.7% exhibiting the lowest sensitivity to applied stress.

Similarly, the R2 PS coefficients for all volume fractions were plotted against strain rate in order to determine the relationship between volume fraction, strain rate, and R2 PS coefficient sensitivity as shown in Figure 5.13 and outlined in Table 5.2.

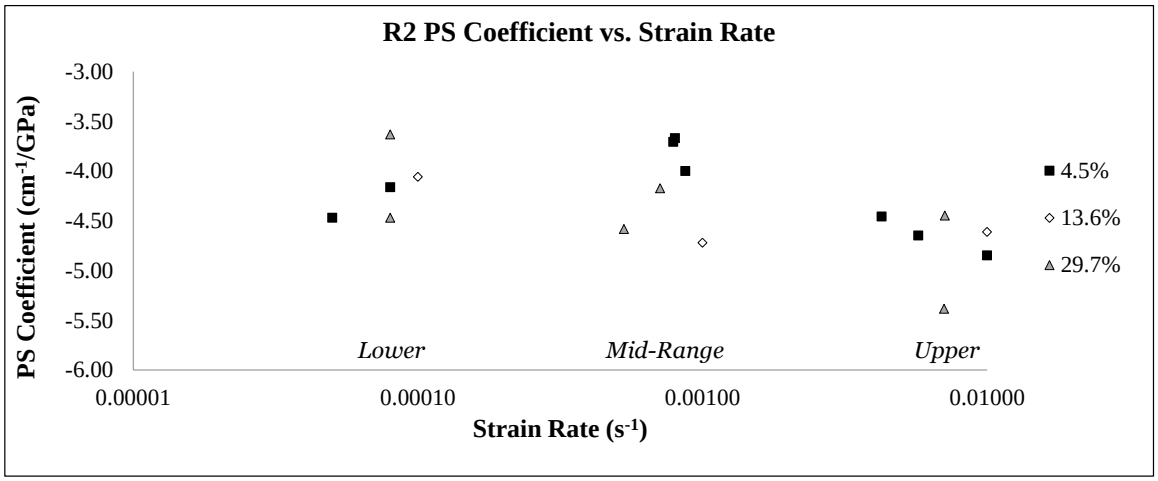

Figure 5.13: R2 PS coefficient dependence on strain rate for all volume fractions

As shown in Figure 5.13 for the lower range of strain rates around $10^{-4}s^{-1}$, R2 PS coefficients for 4.5, 13.6 and 29.7% vary in the range of -3.5 to -4.5 cm^{-1}/GPa with no clear determination of the effect of volume fraction on R2 PS coefficient sensitivity. Similarly, in the upper strain rate region around $10^{-2}s^{-1}$, R2 PS coefficients vary in the range of approximately -4.5 to -5.5 cm^{-1}/GPa with no clear determination of the effect of volume fraction on R2 PS coefficient sensitivity. However, in the mid-range of strain rates

around $10^{-3}s^{-1}$, clear evidence of increasing R2 PS coefficient with increasing volume fraction is presented between 4.5 and 29.7%, as 4.5% has the lowest R2 PS coefficients centralized around -4 cm^{-1}/GPa and 29.7% has higher R2 PS coefficients around -5 cm^{-1}/GPa. In this region, the 13.6% R2 PS coefficient revealed heightened sensitivity to load transfer for R2 of all the volume fractions.

Table 5.2: PS dependence on strain rate for all volume fractions

Volume %	Sample ID	Strain Rate (s^{-1})	R_1 PS Coefficient (cm^{-1}/GPa)	R_2 PS Coefficient (cm^{-1}/GPa)
4.5	1	0.0001*	-3.34	-2.74
	2	0.00008	-4.52	-4.16
	3	0.00005	-4.40	-4.47
	4	0.00087	-4.16	-4.00
	5	0.00079	-3.96	-3.71
	6	0.00080	-3.78	-3.67
	7	0.00426	-4.67	-4.46
	8	0.01*	-4.87	-4.85
	9	0.00573	-4.55	-4.65
13.6	1	0.0001*	-4.30	-4.06
	2	0.001*	-4.41	-4.72
	3	0.01*	-4.26	-4.61
29.7	1	0.00008	-3.77	-3.63
	2	0.00008	-3.15	-2.69
	3	0.00008	-4.54	-4.47
	4	0.00071	-4.39	-4.17
	5	0.00053	-5.37	-4.58
	6	0.00711	-3.61	-4.45
	7	0.00706	-3.40	-5.39
	8	0.00074	-4.46	-2.62

5.5 Discussion of Results

5.5.1 Comparision with Static Results

A comparison between the static and quasi-static PS coefficient ranges for R1 and R2 is shown in Table 5.3.

Table 5.3: Comparison of static and quasi-static PS coefficient magnitude ranges

Volume Fraction		4.5%	5%	13.6%	25%	29.7%	38%
Static	R_1	—	3.16	—	3.65	—	5.63
PS Coefficient	R_2	—	2.6	—	3.42	—	5.08
Quasi-Static	R_1	3.34 - 4.87	—	4.30 - 4.41	—	3.15 - 5.37	—
PS Coefficient	R_2	2.74 - 4.85	—	4.06 - 4.72	—	2.62 - 5.39	—

For 4.5%, the R1 PS coefficients range from -3.34 to -4.87 cm^{-1}/GPa and the R2 PS coefficients range from -2.74 to -4.85 cm^{-1}/GPa, which correlates well with static data for 5% volume fraction, -3.16 cm^{-1}/GPa for R1 and -2.6 cm^{-1}/GPa for R2 [75]. Based on previous work with alumina-epoxy composites under static conditions where the PS coefficient was determined to increase with volume fraction, a composite with

4.5% volume fraction of particles would be expected to have a lower PS coefficient than an composite with 5% volume fraction of particles. Based on the range of PS coefficients for 4.5% presented in this work, 4.5% has improved sensitivity to stress transfer under quasi-static conditions, even considering the lower volume fraction.

In the case of 13.6%, PS coefficients range from -4.30 to -4.41 cm^{-1}/GPa, which are higher than the static values for a 25% volume fraction of -3.65 cm^{-1}/GPa for R1 and -3.42 cm^{-1}/GPa for R2. Based on previous static work, the PS coefficients for 13.6% under static conditions would be expected to have a lower sensitivity in comparison to 25%, however, even considering its lower volume fraction, 13.6% has improved sensitivity to stress transfer under quasi-static conditions.

With PS coefficients ranging from -3.15 to -5.37 cm^{-1}/GPa for R1 and -2.62 to -5.39 cm^{-1}/GPa for R2, 29.7% volume fraction has the largest spread of PS coefficients of all the volume fractions. While sample 5 for 29.7%, tested in the mid-range of strain rates of $10^{-3}s^{-1}$, has an R1 PS coefficient in the range of the 38% static R1 PS coefficient of -5.63 cm^{-1}/GPa [75], generally, the R1 PS coefficients reported for the 29.7% samples tested in this work are lower than the reported static value of -5.63 cm^{-1}/GPa. Similarly, while sample 7 for 29.7%, tested in the upper strain rate range of $10^{-2}s^{-1}$, has an R2 PS coefficient in the range of the 38% static value of -5.08 cm^{-1}/GPa, generally, the R2 PS coefficients reported for the 29.7% samples tested in this work are lower than the reported static value of -5.08 cm^{-1}/GPa. As a result, 29.7% volume fraction samples

generally have decreased PS coefficient sensitivity in relation to the 38% static value, which is expected due to the lower volume fraction.

5.5.2 Variation of PS Properties with Increasing Strain Rates

The effect of strain rate on the PS properties of alumina-epoxy composites of 4.5, 13.6, and 29.7% particle content varies across the strain rate ranges investigated. For 4.5%, R1 and R2 PS properties generally decrease in sensitivity in the lower to mid-range and increase in the mid to upper range. The opposite is true for both 13.6 and 29.7%, where the R1 and R2 PS properties generally increase in sensitivity between the lower to mid-range and decrease in the mid to upper range. While it was expected that the PS coefficient would increase in sensitivity with increasing strain rate, the complex microscale factors ultimately have a large influence on the PS sensitivity results. Factors such as microcracking are most certainly affected by increasing strain rates, which affect the degree of load transfer to the particle modifiers and thus affect the PS sensitivity. In this work, the particle behavior in relation to strain rate was determined, and it was clearly shown that the loading rate does have an impact on the load transfer and resulting PS sensitivity.

5.5.3 Volume Fraction Effect

The volume fraction effect on R1 and R2 PS coefficient sensitivity revealed no distinguishable trend in the lower strain rate region. In the mid-range, it was determined that the R1 and R2 PS coefficient sensitivity generally increases with increasing volume fraction. The upper strain rate range revealed decreasing PS sensitivity with volume fraction for R1 and no distinguishable trend for R2.

Higher volume fractions of alumina-epoxy composites are generally more difficult to manufacture and issues completely dispersing the filler material in the matrix could lead to the presence of agglomerations and voids within the sample. Regions that are not completely homogeneous could cause localized stress concentrations within the sample, resulting in an uneven stress distribution and poor load transfer mechancis. Stress concentrations within the sample would cause the sample to fail prematurely or have high stresses in regions other than the data collection location, thus lending to innaccurate values of PS coefficient sensitivity. In addition to the manufacturing difficulties, higher volume fraction samples inherently have more particles and less matrix material. As a result, there is less binding material within the sample and higher concentrations of ceramic particles, which may also affect the stress distribution of the sample at the microscale.

5.6 Novel Findings

5.6.1 Potential for Failure Monitoring

A novel finding of this work is the potential for failure monitoring using piezospectroscopy as shown in Figure 5.14. The onset of R-line upshifts correlate to the onset of non-linear loading behavior. In compression, R-line upshifts are stress relief to the particles, which may be the result of failure initiation in the form of microcracking and microplasticity. The non-linear loading behavior corresponds to the onset of plasticity or permanent damage to the material. Determining the origination of plasticity in compression through PS R-line upshifts is a promising outcome of this work, which will be further addressed in subsequent studies. This type of early failure detection through the use of alumina-epoxy composites could revolutionize structural health monitoring and mechanics testing in many applications.

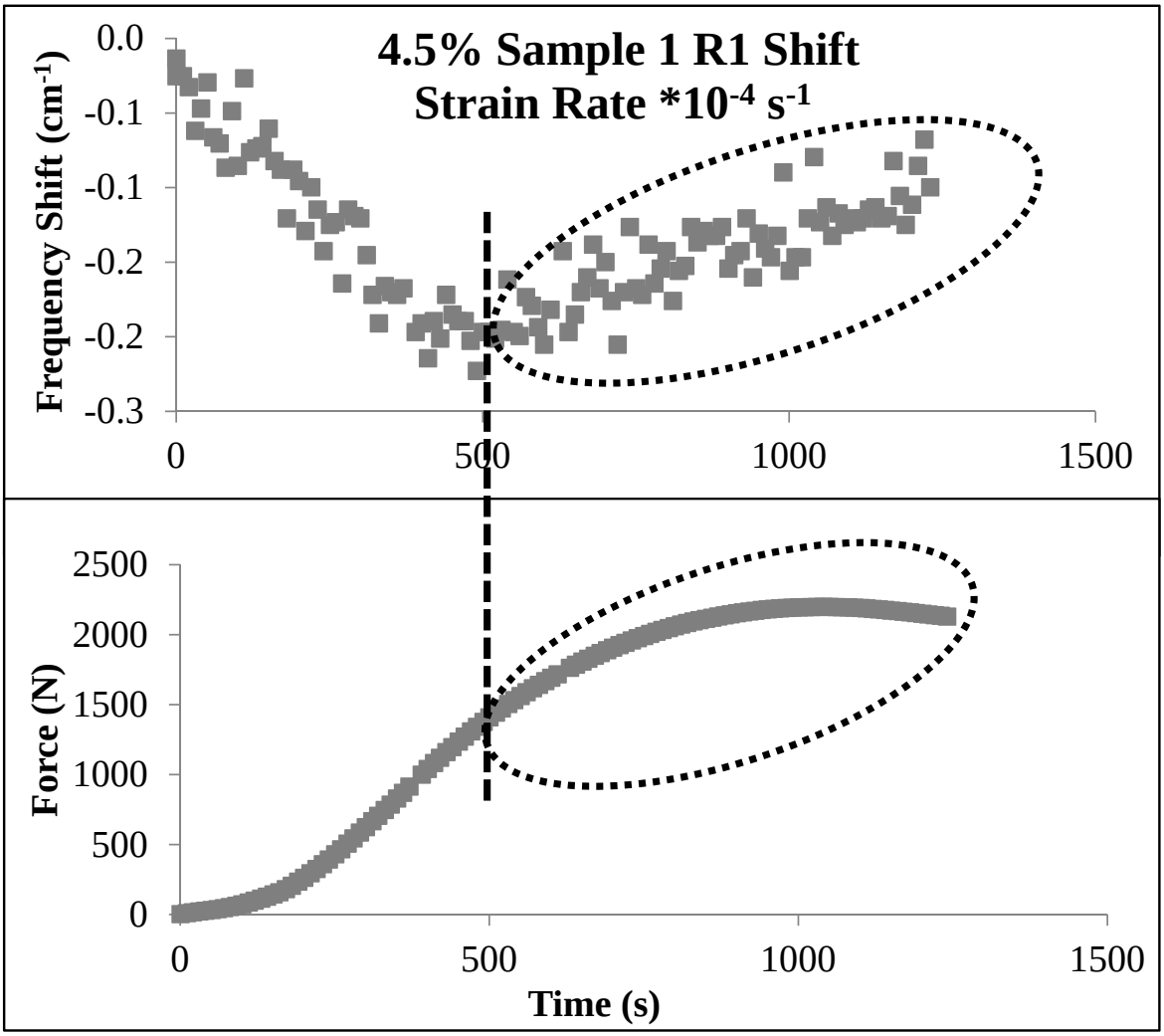

Figure 5.14: Potential for failure monitoring using piezospectroscopy

5.6.2 Potential for Density Compression Collection

Density compression is an important concept to consider when studying materials, especially at variable strain rates. As a material is continuously loaded in compression, a mismatch in the rate of changing dimensions could cause a higher or lower volume fraction of modifiers in relation to an unloaded composite as shown in Figure 5.15. This increase or descrease in volume fraction, even for small changes, can have a significant impact on the material response. A novel finding of this work is the potential to monitor density compression using PSLS. Intensity changes as a function of time can be monitored as shown in Figure 5.15 and compared to a reference calibration to determine the extent of volume fraction changes. However, in order to develop this technique, the laser must remain perfectly focused for the duration of collection, which is a challenge with dynamic deformation that must addressed in future work.

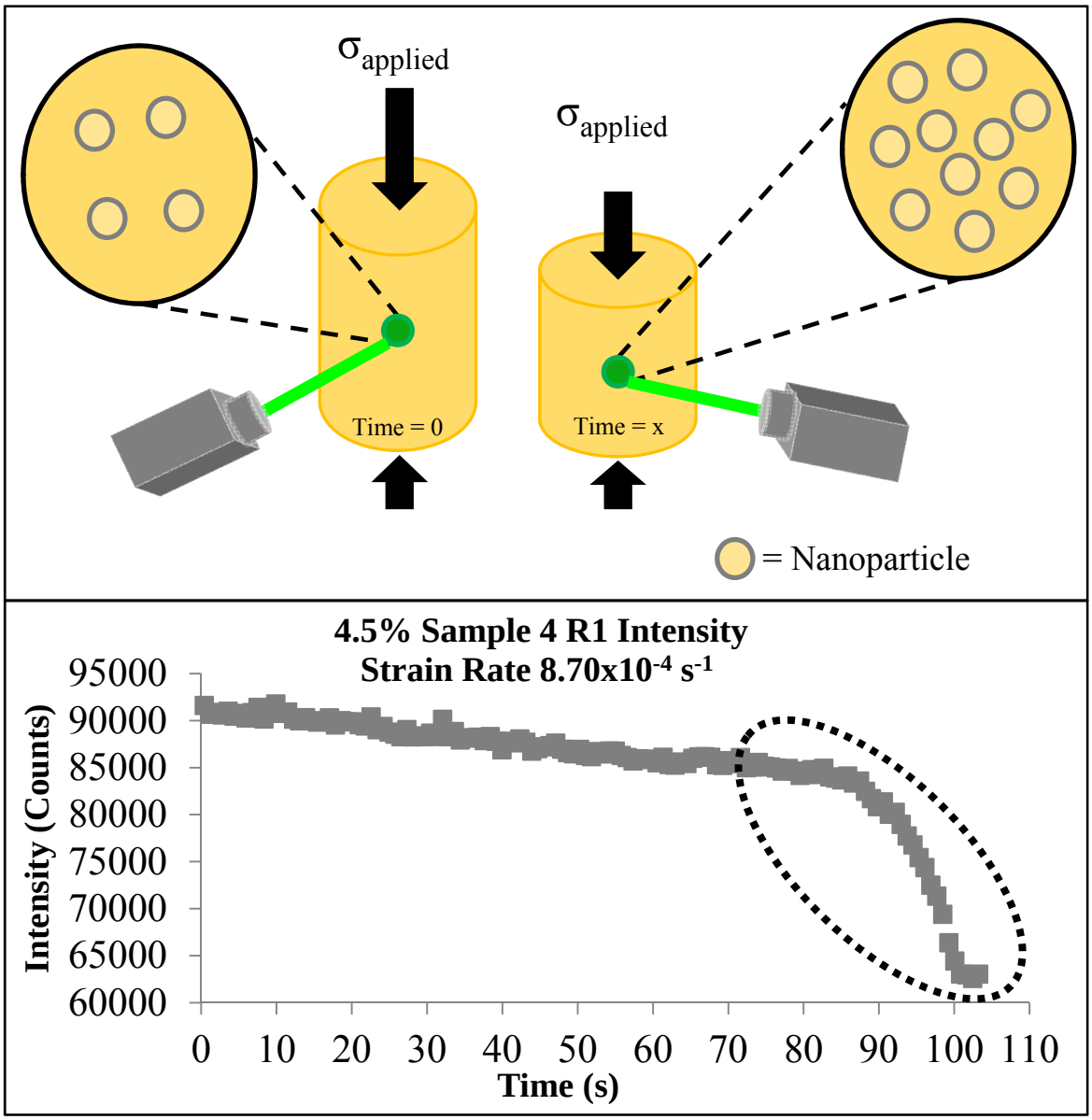

Figure 5.15: Potential to monitor density compression using piezospectroscopy

CHAPTER 6
CONCLUSIONS

Since modifiers, such as alumina nanoparticles, are often added to increase the load carrying capability of a weaker, less stiff matrix material, understanding the load transfer mechanics to the particle is an important and necessary aspect of particulate composite optimization. Small changes in particle size, shape, or volume fraction, or varying the loading rate could substantially change the composite response. However, these types of changes are typically only related to the overall mechanical response of the composite, a macro-scale approach, which is limted due to manufacturing, surface finishing, and experimental testing errors that can skew mechanical test results.

Conventional devices, such as strain gages, have offered a means to collect material information on a smaller scale, however, these devices are limited to discrete locations in the region in which they are attached. Additionally, the differences in load carrying capability of the modifiers and matrix, as individual components, is not ascertained by strain gages as only the overall composite behavior can be determined. These devices collect information from a composite as if it were one homogeneous material, however, in reality particulate composites are a combination of materials, each having a unique mechanical response. Establishing the individual response will serve an important purpose in the design of these particulate composites for optimal properties under the required conditions.

In actuality, the matrix-to-particle and particle-to-particle interactions in particulate composites are innately the mechanisms that lead to improved mechanical properties, such as strength, and are highly affected by loading rate. Results presented in this work through the use of conventional strain gages, revealed improved mechanical strength for increased loading rates. However, these results do not give insight into the particle response, which has been shown to be the response that drives mechanical property improvement.

The use of photo-luminescent alumina particles in an epoxy matrix offerred a solution, as changes in particle stress could be monitored through optical methods, such as piezospectroscopy, by measuring the stress-induced peak shifts of the characteristic R-line peaks present in the emission spectrum of alumina. For the alumina-epoxy composites studied in the work, the ratio of peak shift with applied stress, the PS coefficient, was used to describe the time-dependent particle behavior under quasi-static strain rates. The PS coefficient magnitude described the particle sensitivity to load transfer at each strain rate investigated.

The results illustrate the capability of alumina nanoparticles to act as diagnostic sensors to measure the stress-induced shifts of the spectral R-line peaks resulting from low compressive strain rates. The range of PS coefficients measured, -3.15 to -5.37 cm^{-1}/GPa for R1 and -2.62 to -5.39 cm^{-1}/GPa for R2, correlate well with static test results of similar volume fractions. Results reveal a general trend of increasing sensitivity of the PS coefficients with increasing strain rate when compared to similar materials under

static conditions. In contrast to static results, at a given strain rate, the PS coefficients show varying degrees of sensitivity for each volume fraction. Improvements in composite dispersion, especially at higher volume fractions, and improved curve fitting techniques may lend to improved stress distributions and more accurate R-line peak position shifts.

A novel finding of this work revealed the potential to use piezospectroscopy as a means to monitor early failure in these types of composites through PS upshifts that exist as a result of stress relief to the particle modifiers. Additionally, the potential to use piezospectroscopy as a means to monitor changes in sample density was revealed. These findings and the calibration of the in-situ diagnostic stress-sensing capabilities of varying volume fractions of alumina-epoxy nanocomposites under quasi-static strain rates in this work set the precedent for future studies at high strain rates.

LIST OF REFERENCES

[1] A. Alva and S. Raja. Dynamic characteristics of epoxy hybrid nanocomposites. *Journal of Reinforced Plastics and Composites*, 30:1857, 2011.

[2] R. W. Armstrong and S. M. Walley. High strain rate properties of metals and alloys. *International Materials Review*, 53(3):105–128, 2008.

[3] B. J. Ash, D. F. Rogers, C. J. Wiegand, L. S. Schadler, R. W. Siegel, B. C. Benicewicz, and T. Apple. Mechanical properties of Al_2O_3/polymethylmethacrylate nanocomposites. *Polymer Composites*, 23:1014–1025, 2002.

[4] S. P. Bardakhanov, A. V. Kim, V. I. Lysenko, A. V. Nomoev, D. Y. Trufanov, M. D. Buyantuev, and D. Z. Bazarova. Properties of ceramics prepared from nanopowders. *Inorganic Materials*, 45(3):335–339, 2009.

[5] J. D. Barnett, S. Block, and G. J. Piennarini. An optical fluorescence system for quantitative pressure measurement in the diamond-anvil cell. *The Review of Scientific Instruments*, 44:1–9, 1973.

[6] P. Bhimaraj, D. L. Burris, J. Action, W. G. Sawyer, C. G. Toney, R. W. Siegel, and L. S. Schadler. Effect of matrix morphology on the wear and friction behavior of alumina nanoparticle/poly(ethylene) terephthalate composites. *Wear*, 258:1437–1443, 2005.

[7] R. H. B. Bouma, D. Meuken, and R. Verbeek. Shear initiation of Al/MoO_3-based reactive materials. *Propellants, Explosives, Pyrotechnics*, 32(6):447–453, 2007.

[8] N. K. Bourne, J. C. F. Millett, M. Chen, J. W. McCauley, and D. P. Dandekar. On the hugoniot elastic limit in polycrystalline alumina. *Journal of Applied Physics*, 102:1–9, 2007.

[9] D. L. Burris and W. G. Sawyer. Improved wear resistance in alumina-PTFE nanocomposites with irregular shaped nanoparticles. *Wear*, 260:915–918, 2006.

[10] Q. Chen, I. Chasiotis, C. Chen, and A. Roy. Nanoscale and effective mechanical behavior and fracture of silica nanocomposites. *Composites Science and Technology*, 68:3137–3144, 2008.

[11] N. Chisholm, H. Mahfuz, V. K. Rangari, A. Ashfaq, and S. Jeelani. Fabrication and mechanical characterization of carbon/SiC-epoxy nanocomposites. *Composite Structures*, 67:115–124, 2005.

[12] R. Christensen, D. Lipkin, and D. Clarke. Nondestructive evaluation of the oxidation stresses through thermal barrier coatings using Cr^{3+} piezospectroscopy. *Applied Physics Letters*, 69:3754–3756, 1996.

[13] D. Clarke, R. Christensen, and V. Tolpygo. Evolution of oxidation stresses in zirconia thermal barrier coated superalloy leading to spalling failure. *Surface Coatings and Technology*, 94-95:89–93, 1997.

[14] W. Crossley and E. Williams. A study of adaptive penalty functions for constrained genetic algorithm-based optimization. In *AIAA meeting papers*, 1997.

[15] C. Dancer, H. Curtis, S. Bennett, N. Petrinic, and R. Todd. High strain rate indentation-induced deformation in alumina ceramics measured by Cr^{3+} fluorescence mapping. *Journal of the European Ceramic Society*, 31:2177–2187, 2011.

[16] B. Derby. Ceramic nanocomposites: mechanical properties. *Current Opinion in Solid State and Materials Science*, 3:490–495, 1998.

[17] A. Dorigato and A. Pegoretti. The role of alumina nanoparticles in epoxy adhesives. *Journal of Nanoparticle Research*, 13:2429–2441, 2011.

[18] D. S. Drumheller. On the dynamical response of particulate loaded materials. II. a theory with application to alumina particles in an epoxy matrix. *Journal of Applied Physics*, 53:957–969, 1982.

[19] D. S. Drumheller. *Introduction to Wave Propagation in Nonlinear Fluids and Solids*. The Press Syndicate of the University of Cambridge, 1998.

[20] L. C. Erickson, T. Troczynski, H. M. Hawthorne, H. Tai, and D. Ross. Alumina coatings by plasma spraying of monosize sapphire particles. *Journal of Thermal Spray Technology*, 8:421–426, 1999.

[21] M. Estili, A. Kawasaki, Y. Pittini-Yamada, I. Utke, and J. Michler. *Insitu* characterization of tensile-bending load bearing ability of multi-walled carbon nanotubes in alumina-based nanocomposites. *Journal of materials chemistry*, 21:4272–4278, 2011.

[22] V. M. Evora and A. Shukla. Fabrication, characterization, and dynamic behavior of polyester/TiO_2 nanocomposites. *Materials Science and Engineering*, A361:358–366, 2003.

[23] G. Freihofer, L. Poliah, K. Walker, A. Medina, and S. Raghavan. Optical stress probe: In situ stress mapping with raman and photo-stimulated luminescence spectroscopy. *Journal of Instrumentation*, 5, 2010.

[24] M. Gell, S. Sridharan, and M. Wen. Photoluminescence piezospectroscopy: A multipurpose quality control and NDI technique for thermal barrier coatings. *International Journal of Applied Ceramics Technology*, 1(4):316–329, October 2004.

[25] E. N. Gilbert, B. S. Hayes, and J. C. Seferis. Nano-alumina modified epoxy based film adhesives. *Polymer Engineering and Science*, 43:1096–1104, May 2003.

[26] H. Gleiter. Nanostructured materials: basic concepts and microstructure. *Acta Mater*, 48:1–29, 2000.

[27] L. Grabner. Spectroscopic technique for the measurement of residual stress in sintered Al_2O_3. *Journal of Applied Physics*, 49(5):580–583, 1978.

[28] S. E. Groves, R. J. Sanchez, R. E. Lyon, and A. E. Brown. High strain rate effects for composite materials. *Composite Materials: Testing and Design*, 11:162–176, 1993.

[29] Z. Guo, T. Pereira, O. Choi, Y. Wang, and H. T. Hahn. Surface functionalized alumina nanoparticle filled polymeric nanocomposites with enhanced mechanical properties. *Journal of Materials Chemistry*, 16:2800–2808, 2006.

[30] Y. Gupta and X. Shen. Potential use of the ruby R2 line shift for static high pressure calibration. *Applied Physics Letters*, 58:583–585, 1991.

[31] Y. M. Gupta. Optical stress gauge development for very high stresses piezoraman measurements and analysis. Technical report, Washington State University, 1995.

[32] Y. M. Gupta. Development of optical stress gauges for use in shock wave experiments. Technical report, Washington State University, September 2000.

[33] J. He and D. R. Clarke. Determination of the piezospectroscopic coefficients for chromium doped sapphire. *Journal of American Ceramic Society*, 78(5):1347–1353, 1995.

[34] J. He and D. R. Clarke. Polarization dependence of the Cr^{3+} R-line fluorescence from sapphire and its application to crystal orientation and piezospectroscopic measurement. *Journal of the American Ceramic Society*, 80(1):69–78, June 1997.

[35] P. D. Horn and Y. M. Gupta. Wavelength shift of the ruby luminescence R-lines under shock compression. *Applied Physics Letters*, 49(14):856–858, 1986.

[36] T. Ida, M. Ando, and H. Toraya. Extended pseudo voigt function for approximating the voigt profile. *Journal of Applied Crystallography*, 33:1311–1316, July 2000.

[37] G. C. Jacob, J. M. Starbuck, J. F. Fellers, S. Simunovic, and R. G. Boeman. Strain rate effects on the mechanical properties of polymer composite materials. *Journal of Applied Polymer Science*, 94:296–301, 2004.

[38] B. Johnsen, A. Kinloch, R. Mohammed, A. Taylor, and S. Sprenger. Toughening mechanisms of nanoparticle-modified epoxy polymers. *Polymer*, 48:530–541, 2007.

[39] J. Jordan, B. White, J. Spowart, N. Thadhani, and D. Richards. Static and dynamic mechanical properties of epoxy-based multi-constituent particulate composites. In *DYMAT 2009 - 9th International Conferences on the Mechanical and Physical Behaviour of Materials under Dynamic Loading*, pages 19–25. DYMAT, 2009.

[40] J. L. Jordan, L. Ferranti, R. A. Austin, R. D. Dick, J. R. Foley, N. N. Thadhani, D. L. McDowell, and D. J. Benson. Equation of state of aluminum-iron oxide-epoxy composite. *Journal of Applied Physics*, 101(093520):1–9, 2007.

[41] J. L. Jordan, J. R. Foley, and C. R. Siviour. Mechanical properties of epon 826/DEA epoxy. *Mech Time-Depend Mater*, 12:249–272, 2008.

[42] J. L. Jordan, D. W. Richards, J. E. Spowart, B. White, and N. N. Thadhani. Microstructural design & optimization of highly filled epoxy based composites. Technical report, Air Force Research Laboratory, Munitions Directorate Ordnance Division, 2009.

[43] J. L. Jordan, J. E. Spowart, B. White, N. N. Thadhani, and D. W. Richards. Multifunctional particulate composites for structural applications. *Proceedings of the 11th International Congress and Exposition*, 11:1–9, 2008.

[44] J. F. Kielkopf. New approximation to the voigt function with applications to spectral-line profile analysis. *Journal of the Optical Society of America*, 63:987–995, 1973.

[45] T. Kobayashi, T. Sekine, X. Li, and Y. Yamashita. Observation of wavelength shifts in ruby under shock compression to 36 GPa by time-resolved luminescence spectroscopy. *Physical Review B*, 69(054108):1–7, 2004.

[46] J. Lankford. Compressive strength and microplasticity in polycrystalline alumina. *Journal of Materials Science*, 12:791–796, 1977.

[47] J. Lankford. High strain rate compression and plastic flow of ceramics. *Journal of Materials Science Letters*, 15:745–750, 1996.

[48] J. Lankford, W. Predebon, J. Staehler, G. Subhash, B. Pletka, and C. Anderson. The role of plasticity as a limiting factor in the compressive failure of high strength ceramics. *Mechanics of Materials*, 29:205–218, 1998.

[49] B. Lawn and R. Wilshaw. Review indentation fracture: principles and applications. *Journal of Materials Science*, 10:1049–81, 1975.

[50] D. G. Lee, J. K. Kim, and D. H. Cho. Effects of adhesive fillers on the strength of tubular single lap adhesive joints. *Journal of Adhesion Science Techonology*, 13:1343–1360, 1999.

[51] J. H. Lee, D. Veysset, J. P. Singer, M. Retsch, G. Saini, T. Pezeril, K. A. Nelson, and E. L. Thomas. High strain rate deformation of layered nanocomposites. *Nature Communications*, 3:1164, 2012.

[52] M. Y. Lee, S. K. Ahn, and S. T. Montgomery. Statistical analysis of compositional factors affecting the compressive strength of alumina-loaded epoxy. Technical report, Sandia National Laboratories, February 2006.

[53] P. C. Lysne and C. M. Percival. Electric energy generation by shock compression of ferroelectric ceramics: Normal-mode response of PZT 95/5. *Journal of Applied Physics*, 46:1519–1525, 1975.

[54] Q. Ma and D. R. Clarke. Stress measurement in single-crystal and polycrystalline ceramics using their optical fluorescence. *Journal of the American Ceramic Society*, 76(6):1433–1440, 1993.

[55] Q. Ma and D. R. Clarke. Piezospectroscopic determination of residual stresses in polycrystalline alumina. *Journal of American Ceramic Society*, 77:298–302, 1994.

[56] L. M. McGrath, R. S. Parnas, S. H. King, J. L. Schroeder, D. A. Fischer, and J. L. Lenhart. Investigation of the thermal, mechanical, and fracture properties of alumina-epoxy composites. *Polymer*, 49:999–1014, 2008.

[57] J. C. F. Millett, N. K. Bourne, and D. Deas. The equation of state of two alumina-filled epoxy resins. *Journal of Physics D: Applied Physics*, 38:930–934, 2005.

[58] J. C. F. Millett, D. Deas, N. K. Bourne, and S. T. Montgomery. The deviatoric response of an alumina filled epoxy composite during shock loading. *Journal of Applied Physics*, 102(063518):1–6, 2007.

[59] W. Mock and W. H. Holt. Shock wave compression of an alumina-filled epoxy. Technical report, Armaments Development Department, 1976.

[60] A. K. Mukhopadhyay, K. D. Joshi, A. Dey, R. Chakraborty, A. Rav, S. K. Biswas, and S. C. Gupta. Shock deformation of coarse grain alumina above hugoniot elastic limit. *Journal of Materials Science*, 45:3635–3651, 2010.

[61] D. E. Munson, R. R. Boade, and K. W. Schuler. Stresswave propagation in Al_2O_3 epoxy mixtures. *Journal of Applied Physics*, 49:4797–4807, 1978.

[62] N. Muraki, N. Matoba, T. Hirano, and M. Yoshikawa. Determination of thermal stress distribution in a model microelectronic device encapsulated with alumina filled epoxy resin using fluorescence spectroscopy. *Polymer*, 43:1277–1285, 2002.

[63] C. Ng, L. Scbadler, and R. Siegel. Synthesis and mechanical properties of TiO_2-epoxy nanocomposites. *NanoStructured Materials*, 12:507–510, 1999.

[64] J. Nychka and D. Clarke. Damage quantification in TBCs by photo-stimulated luminescence spectroscopy. *Surface Coatings and Technology*, 146-147:110–116, 2001.

[65] S. Raghavan and P. Imbrie. The development of photo-stimulated luminescence spectroscopy for 3D stress measurements in the thermally grown oxide layer of thermal barrier coatings. In *Proceedings of the Materials Science and Technology 2007 conference*, 2007.

[66] S. Raghavan, P. Imbrie, and W. Crossley. The spectral analysis of R lines and vibronic sidebands in the emission spectrum of ruby using genetic algorithms. *Applied Spectroscopy*, 62:759–765, 2008.

[67] S. Raghavan and P. K. Imbrie. Ex-situ stress measurements in polycrystalline ceramics using photo-stimulated luminescence spectroscopy and high-energy x-rays. *The American Ceramic Society*, 11:1–7, 2009.

[68] R. E. Setchell and M. U. Anderson. Shock-compression response of an alumina-filled epoxy. *Journal of Applied Physics*, 97(083518):1–8, 2005.

[69] R. E. Setchell, M. U. Anderson, and S. T. Montgomery. Compositional effects on the shock-compression response of alumina-filled epoxy. *Journal of Applied Physics*, 101(083527):1–8, 2007.

[70] X. A. Shen and Y. M. Gupta. Effect of crystal orientation on ruby *R*-line shifts under shock compression and tension. *Physical Review B*, 48(5):2929–2940, 1993.

[71] D. K. Shukla and V. Parameswaran. Epoxy composites with 200 nm thick alumina platelets as reinforcements. *Journal of Material Science*, 42:5964–5972, 2007.

[72] R. Siegel, S. K. Chang, A. J. Stone, P. Ajayan, R. W. Doremus, and L. Schadler. Mechanical behavior of polymer and ceramic matrix composites. *Scripta Materialia*, 44:2061–2064, 2001.

[73] B. Song, W. Chen, S. Montgomery, and M. Forrestal. Mechanical response of an alumina-filled epoxy at various strain rates. *Journal of Composite Materials*, 43:1519–1536, 2009.

[74] S. Sridharan, L. Xie, E. H. Jordan, and M. Gell. Stress variation with thermal cycling in the thermally grown oxide of an EB-PVD thermal barrier coating. *Surface Coatings and Technology*, 179:286–296, 2004.

[75] A. Stevenson. Calibration of alumina-epoxy nanocomposites using piezospectroscopy for the development of stress-sensing adhesives. Master's thesis, University of Central Florida, 2011.

[76] A. Stevenson, A. Jones, and S. Raghavan. Characterization of particle dispersion and volume fraction in alumina-filled epoxy nanocomposites using photo-stimulated luminescence spectroscopy. *Polymer*, 43:17, 2011.

[77] A. Stevenson, A. Jones, and S. Raghavan. Stress-sensing nanomaterial calibrated with photostimulated luminescence emission. *Nano Letters*, 11:3274–3278, 2011.

[78] G. Wertheim, M. Butler, K. West, and D. Buchanan. Determination of the gaussian and lorentzian content of experimental line shapes. *Review of Scientific Instruments*, 45:1369–1371, 1974.

[79] B. Wetzel, F. Haupert, and M. Q. Zhang. Epoxy nanocomposites with high mechanical and tribological performance. *Composites Science and Technology*, 63:20552067, 2003.

[80] B. Wetzel, P. Rosso, F. Haupert, and K. Friedrich. Epoxy nanocomposites - fracture and toughening mechanisms. *Engineering Fracture Mechanics*, 73:2375–2398, 2006.

[81] E. Williams and W. Crossley. Empirically derived population size and mutation rate guidelines for a genetic algorithm with uniform crossover. In *Soft Computing in Engineering Design and Manufacturing*, 1998.

[82] H. Z. Wu, S. G. Roberts, and B. Derby. Residual stress distributions around indentations and scratches in polycrystalline Al_2O_3 and Al_2O_3/SiC nanocomposites measured using fluorescence probes. *Acta Materiala*, 56:140–149, 2008.

[83] D. Xie, J. Chung, A. Waas, K. Shahwan, J. Schroeder, R. Boeman, V. Kunk, and L. Klett. Failure analysis of adhesively bonded structures: from coupon level data to structural level predictions and verification. *International Journal of Fracture*, 134:231250, 2005.

[84] Z. H. Xu and D. Rowcliffe. Nanoindentation on diamond-like carbon and alumina coatings. *Surface and Coatings Technology*, 161:44–51, 2002.

[85] M. Q. Zhang, M. Z. Rong, S. L. Yu, B. Wetzel, and K. Friedrich. Effect of particle surface treatment on the tribological performance of epoxy based nanocomposites. *Wear*, 253:1086–1093, 2002.

[86] S. Zhao, L. S. Schadler, H. Hillborg, and T. Auletta. Improvements and mechanisms of fracture and fatigue properties of well-dispersed alumina/epoxy nanocomposites. *Composites Science and Technology*, 68:2976–2982, 2008.

[87] S. C. Zunjarrao and R. P. Singh. Characterization of the fracture behavior of epoxy reinforced with nanometer and micrometer sized aluminum particles. *Composites Science and Technology*, 66:2296–2305, 2006.